UNIVERSITAT POLITÈCNICA DE VALÈNCIA

School of Industrial Engineering

CFD parametric study of battery cells characterization for thermal analysis

Master's Thesis

Master's Degree in Industrial Engineering

AUTHOR: Vanhulle, Ward

Tutor: Margot, Xandra Marcelle

ACADEMIC YEAR: 2022/2023

UNIVERSITAT POLITÈCNICA DE VALÈNCIA

ESCOLA TÈCNICA SUPERIOR ENGINYERIA INDUSTRIAL VALÈNCIA

Parametric study of battery cells characterization for thermal analysis

Ward VANHULLE

Supervised by Professor Xandra Marcelle Margot

Co-supervised by PhD. Kundan Kumar

Academic year 2022-2023

Acknowledgements

First and foremost, I sincerely would like to express my gratitude to my supervisor, Professor Xandra Marcelle Margot, for her unwavering support and guidance throughout the course of my master's thesis. I am truly grateful for the opportunity to pursue this thesis at CMT.

I sincerely appreciate Kundan Kumar, my co-supervisor and PhD candidate, for his unwavering support, tolerance, and commitment. His expertise and willingness to help me surpass my challenges were invaluable. The quality of my work was greatly enhanced by his constructive feedback and thoughtful suggestions.

Also, I am incredibly grateful for the companionship, stimulating discussions and support of my fellow student and roommate during this exciting semester studying abroad. His presence made this journey even more enjoyable, and unforgettable.

Additionally, I would love to thank my family from the bottom of my heart for their unconditional love and support. Their encouragement, empathy and trust in my abilities have been crucial to my education. I am truly grateful for their constant presence in my life.

Lastly, I would like to thank my girlfriend and my friends for their motivation, love, and goodwill. Their presence and support have made this academic journey more fulfilling and pleasant.

I am blessed and grateful to have had such wonderful individuals in my life who have contributed to the successful completion of my master's thesis. Without their guidance, support, and encouragement this project would have been very hard. I am truly fortunate to have had them by my side, whether offline or online.

Thank you all.

Ward Vanhulle

Summary

Keywords: battery cell, thermal conductivity, battery cell structure, heat generated, CFD.

This master's thesis deals with the thermal study of a cylindrical LiFePO4-32700-6Ah battery cell. One of the problems when trying to calculate the heat generated by a cell is the determination of the thermal conductivity and capacitance of the cell. The manufacturers do not provide this information. Since for nodal models, as well as for CFD models, the thermal conductivity is an input parameter, it can be calculated from Fourier's law, provided that the layered structure is known (material, the thickness of each layer, number of layers, etc.). However, there is hardly any information about the layered structure of a cell. Therefore, this work aims to perform a parametric study of the cell structure by varying the electrode, anode, and cathode material thickness to analyse the effect on the thermal conductivity, specific heat, and density of the cells. These parametric values will be fed into the CFD cell model, and the results of the simulations will be compared with the available experimental data.

Resumen

Palabras clave: celda de batería, conductividad térmica, estructura de celda de batería, calor generado, CFD.

La tesis de master trata sobre el estudio térmico de una celda de batería cilíndrica LiFePO4-32700-6Ah. Uno de los problemas, cuando se trata de calcular el calor generado por una celda, es la determinación de la conductividad y capacitancia térmica de la celda. Los fabricantes no proporcionan esta información. Dado que para los modelos nodales, así como para los modelos CFD, la conductividad térmica es un parámetro de entrada, esta se puede calcular a partir de la ley de Fourier, siempre que se conozca la estructura de las capas (material, espesor de cada capa, número de capas, etc.). Sin embargo, apenas hay información sobre la estructura de las capas de una celda. Por lo tanto, el objetivo de este trabajo es realizar un estudio paramétrico de la estructura de la celda, variando el espesor del material de los electrodos, ánodo y cátodo para analizar el efecto sobre la conductividad térmica, el calor específico y la densidad de las celdas. Estos valores paramétricos se introducirán en el modelo de celda CFD y los resultados de las simulaciones se compararán con los datos experimentales disponibles.

Table of content

List of symbols

c_p	[J·kg^{-1}·K^{-1}]	: Specific heat capacity
j	[A·mm^{-2}]	: Current density
k	[W·m^{-1}·K^{-1}]	: Thermal conductivity
q	[W]	: Heat
$\dot{q}$	[Wh]	: Heat generation
r	[mm]	: Radius
t	[s]	: Time
A	[mm²]	: Area
C	[F]	: Capacitance
C_{th}	[J·kg^{-1}]	: Thermal capacity
I	[A]	: Current
L	[mm]	: Length
N	[/]	: Number of cell layers
Q	[Ah]	: Charge capacity
R	[Ω]	: Resistance
SOC	[/]	: State of charge
T	[°C]	: Temperature
U	[V]	: Potential
V	[V]	: Voltage
Vol	[mm³]	: Volume

Greek symbols

δ	[µm]	: Thickness
ρ	[kg·mm³]	: Density
σ	[S·m^{-1}]	: Electrical conductivity
φ	[V]	: Phase potential

Subscripts

1	: First
$+$	: Positive
$-$	: Negative
$abuse$	: Abuse
ax	: Axial
c	: Current collector
e	: Electrode

eq	: Equivalent
Ech	: Electrochemical
$i-1$	: Previous
$i+1$	: Next
i	: i^{th} material layer
n	: Outer/last layer
$n-1$	: Second last layer
nom	: Nominal
N_c	: Negative current collector
N_e	: Negative electrode
ocv	: Open-circuit voltage
$parallel$	: In parallel
P_c	: Positive current collector
P_e	: Positive electrode
rad	: Radial
ref	: Reference
s	: Separator
$series$	: In series
$short$	: Short-circuit
th	: Thermal
$total$	: One cell layer
$total(N_c, N_e)$	: total for negative components
$total(P_c, P_e)$	: total for positive components

Superscripts

N	: Negative
P	: Positive

List of abbreviations

CAD	: Computer-aided design
CFD	: Computational fluid dynamics
DOD	: Depth of discharge
DOE	: Design of experiments
ECM	: Equivalent circuit model
EV	: Electric vehicle
HEV	: Hybrid electric vehicle
ICEV	: Internal combustion engine vehicle
LCO	: Lithium cobalt oxide
LFP	: Lithium ferro phosphate
LTO	: Lithium titanate oxide
LMO	: Lithium manganese oxide
MSMD	: multi-scale multi-domain
N_c	: Negative current collector
N_e	: Negative electrode
NASICON	: Natrium superionic conductor
NCA	: Lithium nickel cobalt aluminium oxide
NMC	: Lithium nickel manganese cobalt oxide
P_c	: Positive current collector
P_e	: Positive electrode
PNZ	: Pathway to net zero emissions
S	: Separator
SEI	: Solid electrolyte interface
SOC	: State of charge

1 INTRODUCTION

1.1 Contextualization and purpose of the work

The global focus on reducing greenhouse gas emissions by using renewable energy sources increases rapidly. This plays an important role in industries such as power generation and automotive. From this perspective, batteries have gained significant popularity because of their wide range of applications. They can be used for EVs, smart grids and energy storage. Currently, the lithium-ion battery is studied the most extensively [1].

In the automotive sector, the battery pack is a crucial part of the success of EVs. It provides the required energy to power the electric motor. To achieve the desired characteristics of the battery pack, multiple cells are interconnected in series, parallel or a combination of both. In turn, these properties partially impact the specifications of the car, such as the vehicle range, acceleration, and durability. Thus, the battery performance needs to be adequate and consistent. However, the performance output can be majorly affected by temperature, such as the rise of the cell temperature during charging or discharging conditions [2].

Therefore, it is important to know the temperature distribution in a cell before implementing it in a battery pack. Moreover, the cell's thermal behaviour depends on the material properties of the layers inside it. Since manufacturers do not provide information about the inner cell structure (only the materials are known), this thesis investigates a method for determining the thickness of those layers, without the adequate process of cutting a battery cell to determine its internal configuration. Once the internal configuration is determined, the thermal behaviour of one cell will be characterized.

This master's thesis is conducted at CMT, located on the campus Vera from the UPV – Universitat Politècnica de València. The inspiration for the process of this master's thesis comes from the need to characterize the cell thermal behaviour and temperature distribution for further thermal management purposes.

1.2 Workflow

For this master's thesis, the workflow is described in Table 1-1 underneath. It represents the steps taken to conduct the research while guarding the quality of the work. This gives an overview of the chronological order of the steps taken to investigate the subject of this thesis.

Table 1-1: Workflow description.

Description of the activity	2023			
	February	March	April	June
Comprehending the assignment.				
Assessing the scope of the project in consultation with the supervisor.				
Theoretical study on Li-ion battery cells.				
Study of thermal characteristics of Li-ion cells.				
Determine the thermal parameters of the cell in function of the cell structure using a novel approach.				
Set up the CFD models.				
Validation of the used approach.				
Define DOE to determine which material thicknesses have a significant impact on the cell's thermal behaviour.				
Perform DOE CFD calculations and analyse results.				

1.3 Outline

This research project is organised in a particular sequence of six parts, each with a specific purpose:

Chapter 1 illustrates the general direction and briefly introduces the theme of the work.

Chapter 2 deals with the operation of lithium-ion batteries. Also, a brief review is given of existing literature concerning the thermal aspects, and internal configuration associated with the cells.

Chapter 3 details the setup of the experiments performed using empirical data of interest. The details include the theoretical fundament of the performed calculations as well as the set-up of the CFD simulations. It also includes the analysis of any relationships, equations and assumptions utilized in the research.

Chapter 4 analyses the results from the conducted experiments generated in chapter 3.

Chapter 5 represents the conclusions made from this research and suggests recommendations for further investigations.

Chapter 6 gives an overview of the budget to execute the research done for this master's thesis.

2 BACKGROUND AND LITERATURE REVIEW

2.1 Future predictions for energy

Since the world is pacing amazingly fast in terms of energy, some predictions of energy have been made. The energy transition outlook by DNV forecasts a prediction until 2050 [3]. The report predicts a tremendous shift in global energy over the next three decades. The statements are limited to the topic of this work, which revolves mainly around electrical energy.

2.1.1 Highlights

The most crucial point of the DNV report is the feasibility of keeping global warming under the target of 1,5°C set by the Conference of the Parties agreed under the Paris Agreement. It is strongly believed that the currently available technologies have the potential to reach this goal. However, the report states this will only be possible under strictly enforced policies to push technologies beyond boundaries. The window to act on this target is closing and securing 1,5°C is already impossible without a temporary carbon overshoot. The most likely energy future results in global warming of 2,2°C by the end of the century as seen in Figure 2-1.

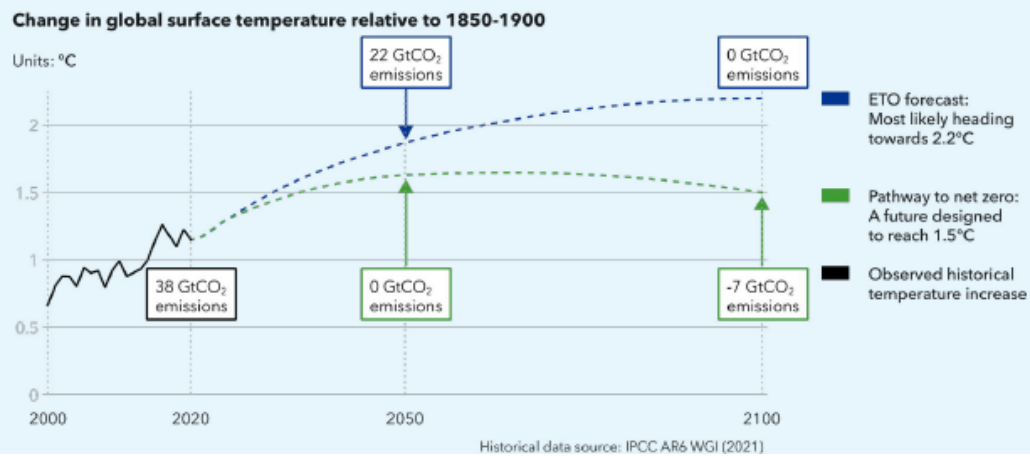

Figure 2-1: Global temperature evolution [3]**.**

Figure 2-2 shows a forecast of the primary energy until the year 2050. Energy usage will peak within the next three decades, more precisely in 2036 at a level 8% higher than today. The main reason for the decline later than 2036 is the electrification of the energy supply. This provides higher energy density and intensity, which means the energy services can over time be delivered with less use of primary energy. The share of the electricity demand will more than double by 2050 and grow at 3% per year. The biggest factor for this fast-paced growth lies in the electrification of road transport. Globally, half the pack of passenger vehicles are predicted to be EVs by the beginning of the 2030s. Oil will gradually decrease after reaching a peak of 15% above 2023's level in 2025, eventually 32% lower in 2050. Natural gas on the other hand peaks in 2036 and will surpass oil as the largest source of primary energy. In 2050, just 12% of gas will be carbon-free. Electricity will remain the mainstay of the transition as it's growing and greening everywhere [3].

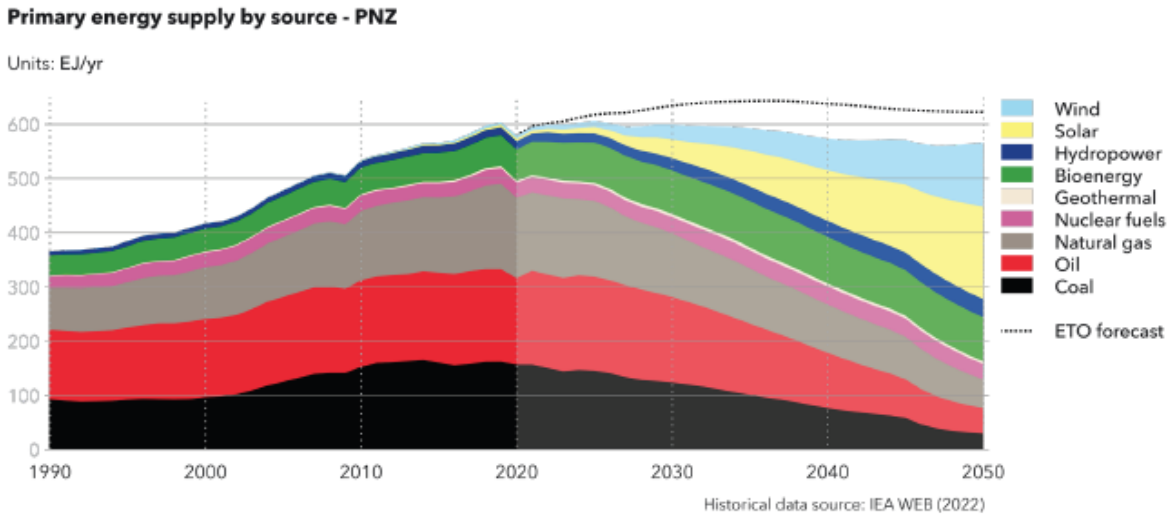

Figure 2-2: Primary energy and its related sources [3]**.**

2.1.2 Electricity

In much of the developing world, the fundamental motor of the energy shift is electrification which has a favourable impact on access to clean energy. Electricity represented only 19% of the world's final energy use in 2021. By 2050, this will almost double to 36%. The biggest advantage of electricity is its higher efficiency in its end use. Demand will rise from 27PWh/yr. to 62PWh/yr. and nearly 70% of that will be supplied by wind and solar PV energy.

Figure 2-3 represents the evolution of the global electricity demand by sector. Not all demand sectors have the same growth trajectories. For example, the biggest growths in demand will be for transport, hydrogen production and space cooling. In the energy transition outlook, it is stated that electricity demand for appliances and lightning will increase by two times by 2050, compared to 2022. This is due to the electrification of under-electrified regions, such as Sub-Saharan Africa and the Indian Subcontinent. Most electricity in the industry is used either as heat or to run machines, motors, and other appliances.

As can be seen from Figure 2-4 the increased electricity generation will be through wind and solar in the coming decades, thus, it is important to bridge the gap when the availability of the sun or wind is not enough for energy production. In such scenarios, batteries can play a vital role in bridging these moments releasing energy that was stored in times of overproduction. In this way, it is still possible to follow the energy demand even when the energy generated by wind or sun is not sufficient. Batteries are a great alternative for energy storage in the form of pumped hydro. The main disadvantage of pumped hydro is the geographical limitation. On top of that it is forecast to only provide a marginal increase in the dramatically added requirement to power storage over the next thirty years. Talking about batteries today, Li-ion is the most dominant technology for utility-scale storage. The cost of such batteries increased during and after the pandemic, but predictions say the cost will reduce by 80% between 2023 and 2050. In that way, electricity will eventually become cheaper relative to other fuels [3].

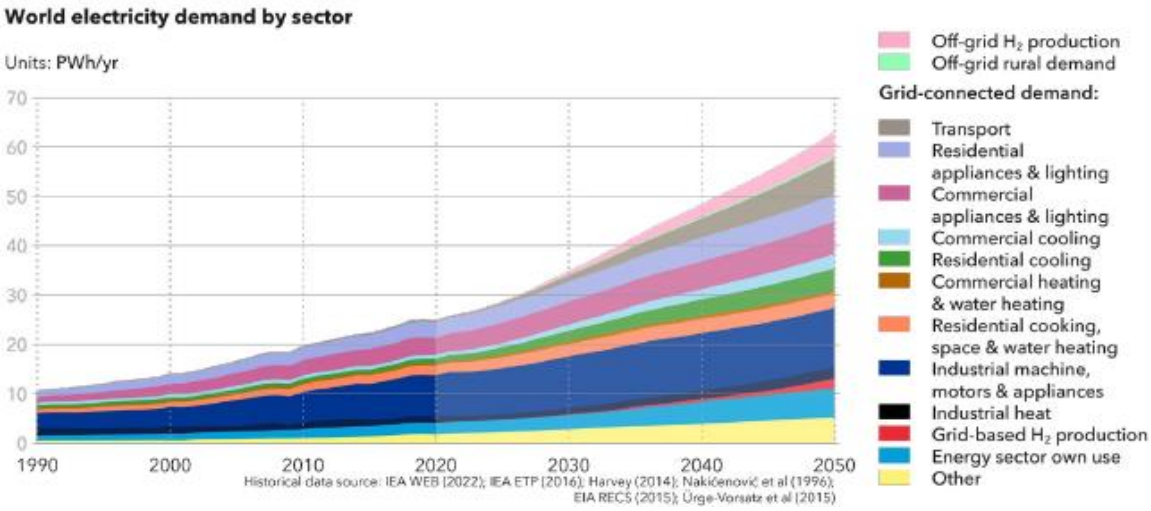

Figure 2-3: Global electricity market demand [3]**.**

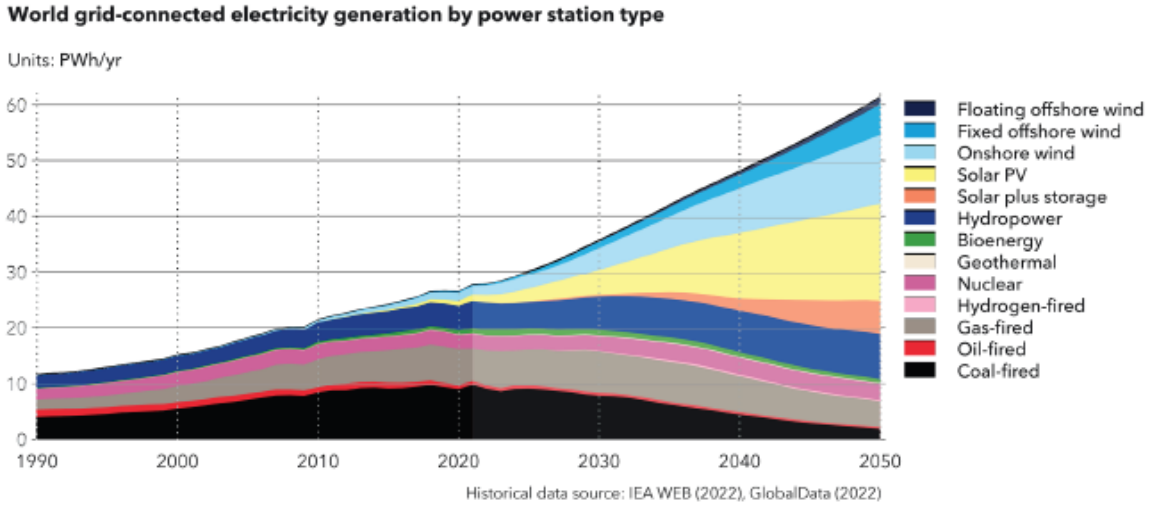

Figure 2-4: Grid electricity by generation source [3]**.**

2.1.3 Road transport

Underneath some comments are made regarding Figure 2-5, which represents that fuel cell electric vehicles are much less efficient and more complicated, thus more costly than battery electric vehicles. This is why the future landscape for passenger transport will grow to an 85% share of battery-electric vehicles. Regarding the pathway to net zero emissions (PNZ), fossil-fuelled vehicles will be subject to much stricter fuel economy standards to reduce fuel consumption to a minimum. To boycott the use of fossil fuels, taxation levels will increase between +75% and +200% compared to the current level. This will cause internal combustion engines to drop by 66% over the next three decades, while battery electric vehicles grow by 27% as Figure 2-5 describes.

The fundamental technologies required to achieve this pathway already exist. The primary tool for reducing emissions in passenger vehicles is the replacement of ICEVs with BEVs. Once built, EVs are roughly three times more efficient than ICEVs. Furthermore, as more renewables are added to the power mix, EVs become less emission-intensive. The development of lithium-ion battery configurations will improve the battery charging speed and total power capacity, thus efficiency and range of the vehicles. Eventually, the charging speed of charging stations has no other choice than to follow these developments.

These advantages of electric propulsion will edge out both fossil fuels and hydrogen in passenger vehicles as well as in the short to medium-term [3].

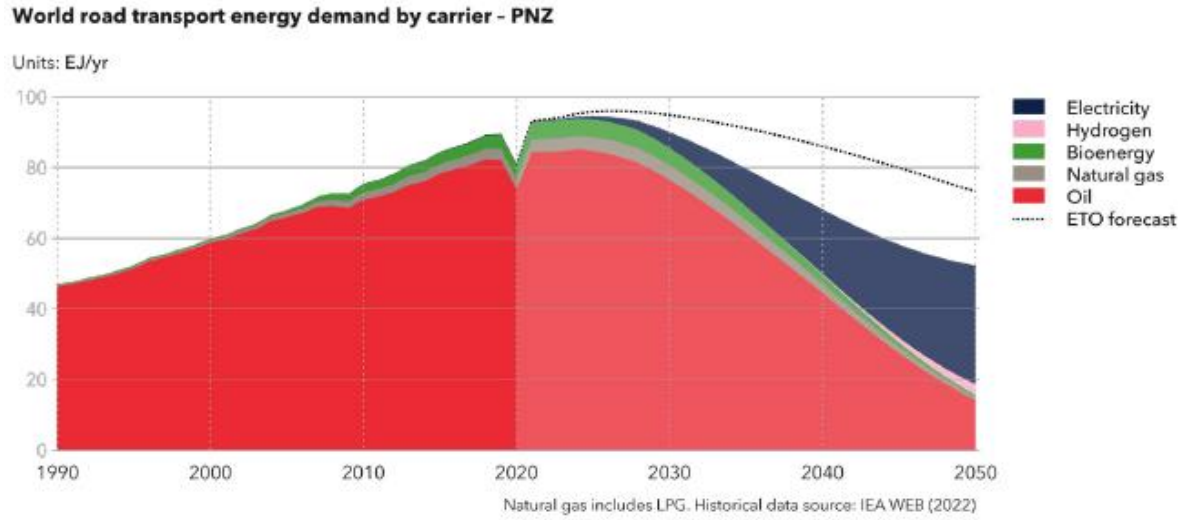

Figure 2-5: Energy demand for transportation by its carrier [3]**.**

2.2 Introduction to batteries

A battery is a device that uses electrochemical reactions, reduction and oxidation, to store and convert chemical energy into electrical energy. This was first shown and quantified, based on the experiments Galvani did, by the Italian scientist named Volta through his invention, the voltaic pile. The pile consists of two distinct metal disks, zinc, and silver, separated by porous cardboard in a solution of saltwater. This configuration allowed a controlled flow of electrical current connecting both metal electrodes [4].

Furthermore, batteries are classified into three types: primary, secondary, and reserve. The first type is a galvanic cell composed of chemical materials that cannot be recharged electrically. As a result, they can only be used for one discharge cycle before becoming obsolete and discarded. Most of today's batteries are secondary or rechargeable batteries designed to be used for multiple cycles. They can be recharged by an external electrical source, making them more cost-effective than replacing primary batteries in frequently used applications [5]. Thirdly, in reserve batteries, also called stand-by batteries, the electrolyte is generally stored apart from electrodes and inserted when a sudden high amount of energy is needed. Separate storage eliminates the possibility of self-discharge prior to use. This type of battery is commonly used in applications that require a high amount of power for a brief time for activation of a process. The main examples are weapon systems, missiles or torpedoes [6]. As this thesis' subject is focused on secondary batteries, wherever the word battery is used, it means secondary, rechargeable battery.

2.2.1 Secondary batteries

Figure 2-6 shows the secondary battery's energy density over time. Over the past two centuries, three stages can be distinguished. During the first stage, or as Warner et al. [7] call the 'Industrial Age', the earliest batteries were used to help to power the budding technologies from the global Industrial Revolution era. During these nearly 100 years, the manufacturing processes were improved, and the cycle life was increased, however, improvement lacked in energy density. The next stage calls the 'Portable Age' by Warner et al. [7], coincides with the introduction of the cell phone, smartphone, computer, and many other technologies. This stage brought advancement in lithium-ion battery technology by enabling it to power the abovementioned tools while being a portable device. From 2009 and still going, the 'Mobile Age', batteries became so energy-dense, they became capable of fully electrifying vehicles [7].

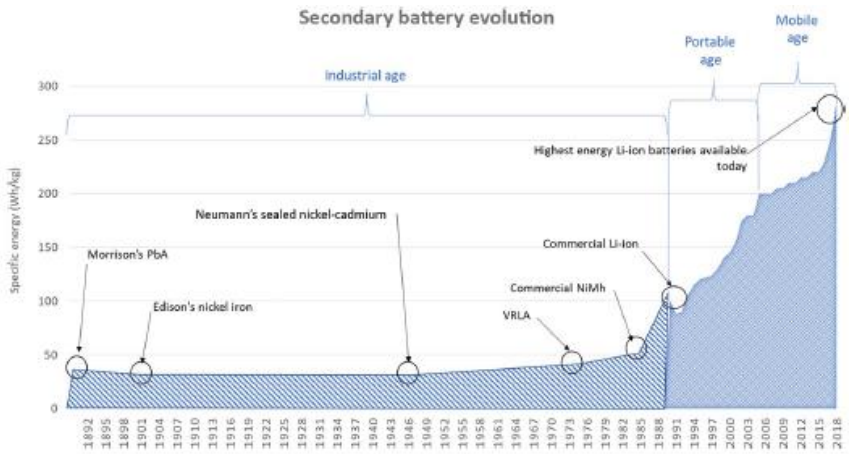

Figure 2-6: Modern battery-specific energy over time [7].

2.2.2 Why lithium?

A big benefit of lithium is the fact that it is the lightest metal on the planet. Just like other alkali earth metals, lithium is highly reactive. The combination of the previous characteristics of lithium means that it is much more energy dense than other metals, which is especially useful for storing energy. Derived from its atomic number, lithium only got three electrons circling in two bands around the core of three neutrons and protons. Valence electrons are situated on the outer band. For lithium, there's only one valence electron. On this outer band, there are spots left for free electrons swerving in the neighbourhood of the lithium atom. Lithium can reject its only valence electron to become a positive ion or cation. Or it can accept another free electron to contain more electrons than protons to become negatively loaded, an anion is created. For battery applications, it is highly desirable to find a light chemical element with the ability to alternate between cations and anions. Because of its properties, lithium participates effectively in the movement of charges due to the electrochemical reactions within the battery cell. The above characteristics made lithium the dominant choice for battery design [7].

2.3 Working principles of a Lithium-ion Battery

A lithium-ion battery works by using the movements of lithium-ions to store and provide energy. The lithium ions are trapped between two electrodes. For further explanation of the operation of such cells, a $LiFePO_4$ battery is chosen as this thesis focuses on LFP batteries. One of the electrodes is made of lithium iron phosphate, $LiFePO_4$, while the other one consists of carbon, C. By extracting lithium out of the metal grid, it automatically splits into a lithium-ion and an electron. By guiding these free electrons over an external circuit, current will flow, defined in the opposite direction, which can be used to power a device or recharge the battery. Current flows per definition from the positive pole toward the negative pole of the power supply. The current field is created by the electron flow through the current collector. Since the polarity of electrons is opposite to the polarity of the ions, they flow in the other direction. The ions flow between the electrodes, crossing the electrolyte and separator [8]–[10].

2.3.1 Discharging conditions

When a load is applied to the external circuit, it drains energy from the battery. When discharging, the load pulls electrons from the positive terminal out of the battery toward itself. To provide these electrons the oxidation reaction occurs at the anode [7], [11]. The electrochemical reaction on the anode side is represented as:

$$LiC_6 \rightarrow Li_{1-x}C_6 + x \cdot Li^+ + e^- \qquad (2\text{-}1)$$

The anode loses negatively charged electrons, making it the positive terminal. Meanwhile, the cations of lithium diffuse through the separator toward the cathode. At the cathode, the cations and the electrons eventually come back together to intercalate in the metal grid. Only a reduction reaction can employ the electrons arriving at the cathode to prevent them from accumulating there, as the electrolyte doesn't allow any flow of free electrons [7], [11], as it is portrayed in the equation (2-2).

$$x \cdot LiFePO_4 + x \cdot Li^+ + x \cdot e^- \rightarrow LiFePO_4 \qquad (2\text{-}2)$$

The anode gains negatively charged electrons, making it the negative terminal. The discharging process is graphically shown in Figure 2-7.

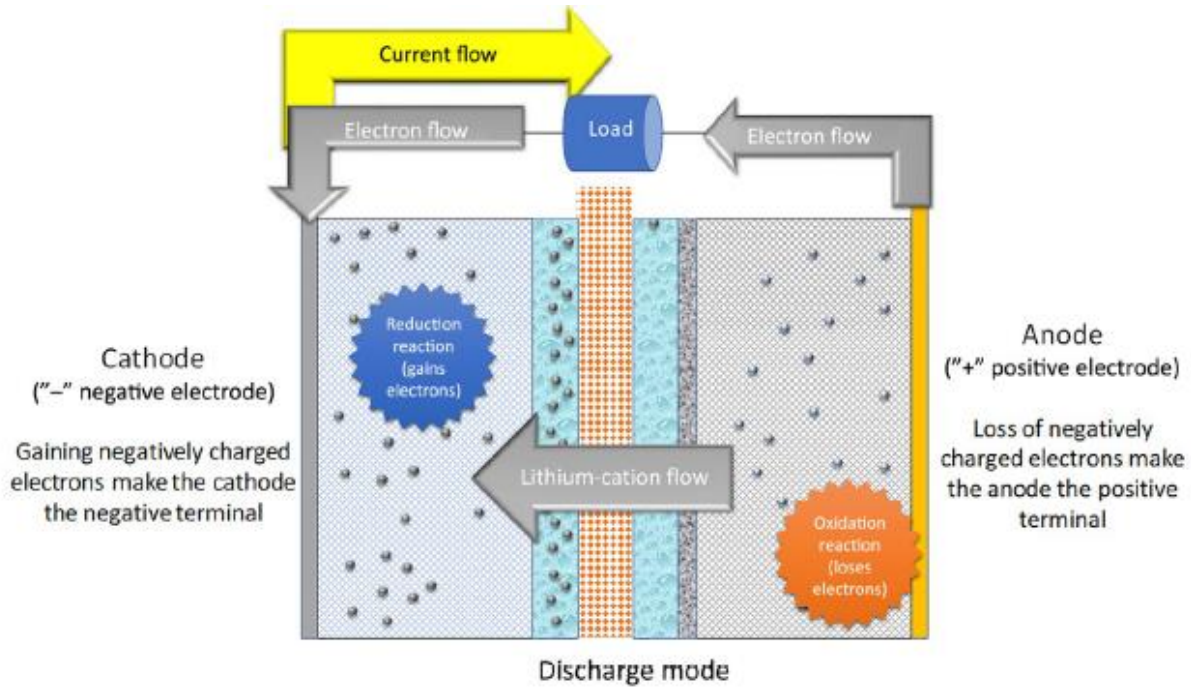

Figure 2-7: current flow during discharge mode [7]**.**

2.3.2 Charging conditions

When charging, a power source is applied to the external circuit to reverse the reactions and create a current flow in the opposite direction. It provides the energy needed to break the lithium-ions out of the metal grid. The oxidation reaction occurs [7], [11]:

$$Li_mFePO_4 \rightarrow Li_{1-x}FePO_4 + x \cdot Li^+ + x \cdot e^- \qquad (2\text{-}3)$$

The cathode loses negatively charged electrons, making it the positive terminal. Positively charged lithium-ions, cations, migrate from the cathode through the separator, to the anode where these intercalate in the graphite. Eventually, the ions and electrons, supplied through the external circuit, come together at the anode. The anode gains negatively charged electrons, making it the negative terminal. At the anode, the reduction reaction takes place [7], [11]:

$$Li_{1-x}C_6 + x \cdot Li^+ + x \cdot e^- \rightarrow LiC_6 \qquad (2\text{-}4)$$

This process replenishes the lithium ions consumed during the discharge cycle and restores the battery's storage capacity. Figure 2-8 displays the charging process.

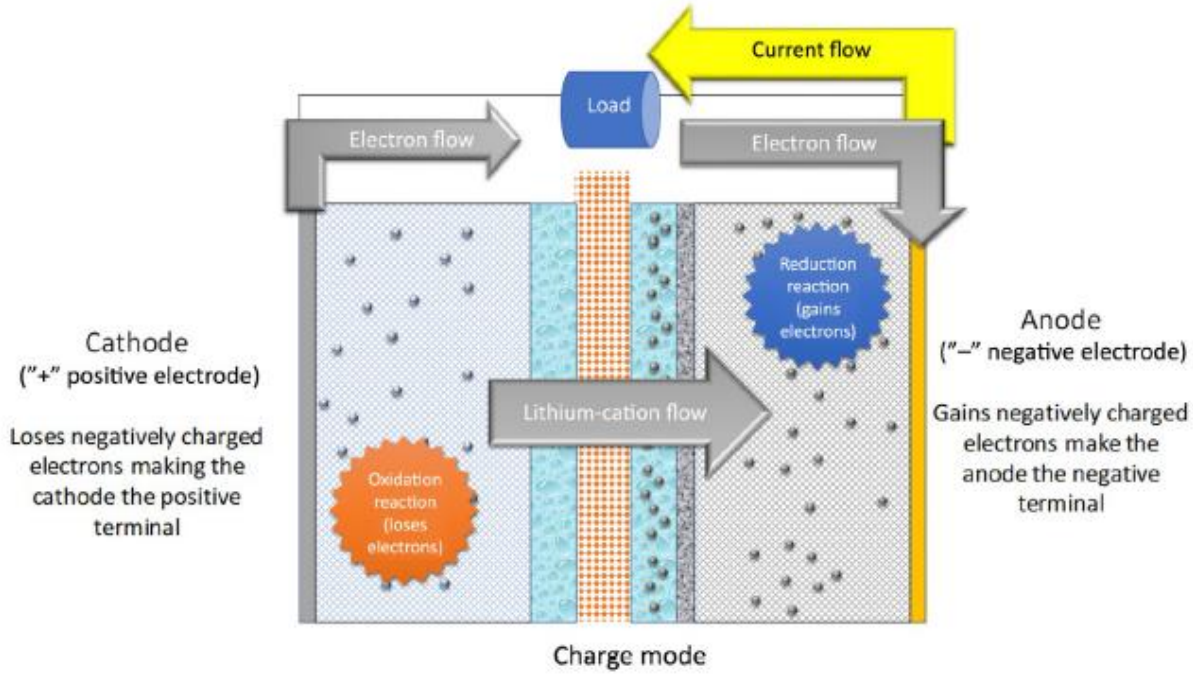

Figure 2-8: current flow during charge mode [7]**.**

2.3.3 Solid electrolyte interface layer

When a lithium-ion battery is charged and discharged for the first time, a chemical reaction takes place between the anode and the electrolyte. During this reaction, a protective layer is created at the boundary between these, which is known as the solid electrolyte interface or SEI [7]. For the first few charge and discharge cycles, when the electrolyte meets the electrode, solvents in an electrolyte, which are accompanied by the lithium ions during charging, react with the electrode and start to decompose. This decomposition results in the formation of LiF, Li_2O, LiCl, and Li_2CO_3 compounds. These components precipitate on the electrode and form a few nanometre-thick layers called solid electrolyte interface (SEI). During the irreversible formation of the SEI layer, a certain amount of electrolyte and lithium ions are permanently consumed. Thus the consumption of lithium ions during the formation of SEI results in a permanent loss of capacity [12].

Without the generation of a stable SEI, lithium-ion batteries could not be reversibly charged and discharged. To be effective, the SEI must be lithium-ion conducting to allow lithium-ion transport through the layer and into the negative electrode, but it must also be electronically insulating to prevent the continuous reduction of the electrolyte. Moreover, it also needs to be chemically, thermally and mechanically stable while being only a few nanometres thick [13].

2.4 Battery components

Figure 2-9 shows the cross-section of a standard lithium-ion cell. The following layers are distinguished: current collectors, electrodes, electrolyte, and separator. Inside the electrodes, anode and cathode, the electrochemical reactions take place as described in 2.3.1 and 2.3.2. The current collectors, one for each pole, conduct the released electrons to the external circuit so that current flows and the electrical energy can be transferred. The two poles of the cell are divided physically by the separator within the electrolyte. It is a semi-permeable wall, which only allows the flow of ions. The electrolyte facilitates the transport of the ions between the anode and cathode. This flow is crucial for maintaining the charge balance during the electrochemical reactions. Between the anode and the electrolyte an SEI layer is formed during the first charge and discharge cycles of the battery cell, which was further described in 2.3.3.

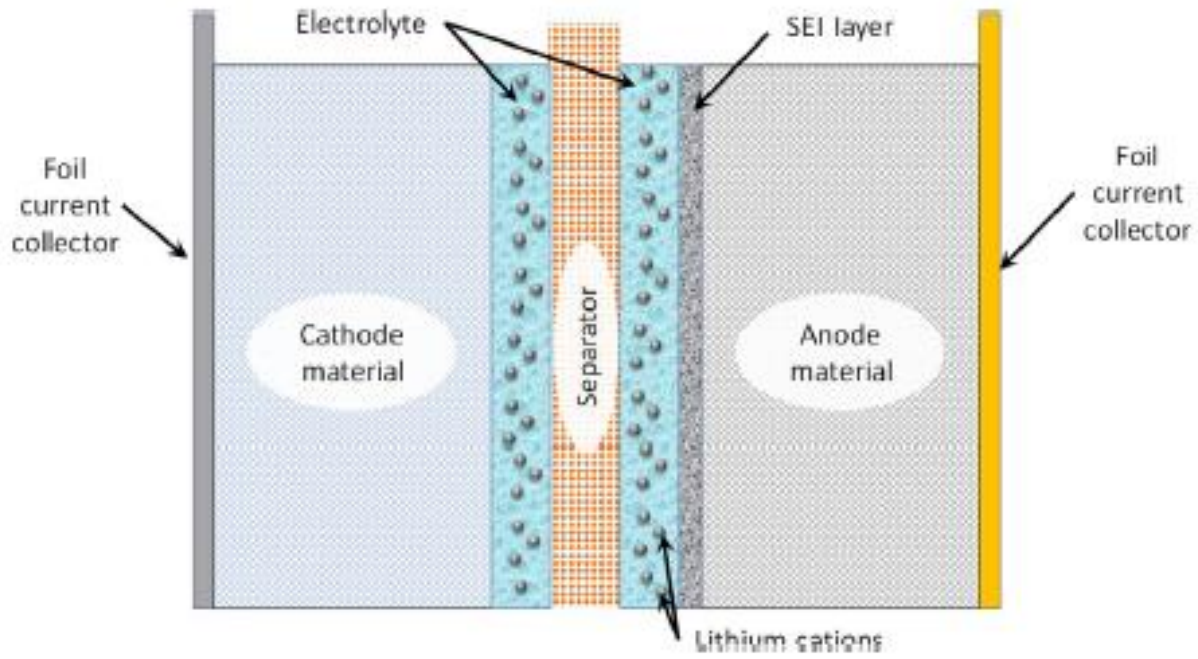

Figure 2-9: cross-section of a lithium-ion cell [7]**.**

2.4.1 Cathode electrode chemistries

The cathode comprises three parts: the active material where the electrochemical reactions take place, the current collector which collects the electrons and conducts them as current to the load outside the battery, and the conductive binder, which holds the other two parts together and lets the electrons pass. Numerous commercially available lithium-based electrode pairs have been identified. The active material at the cathode consists of a lithiated metal oxide or -phosphate. Underneath the three most common chemistries for the cathode are discussed. Usually, the type of lithium-ion cell is defined by the cathode material.

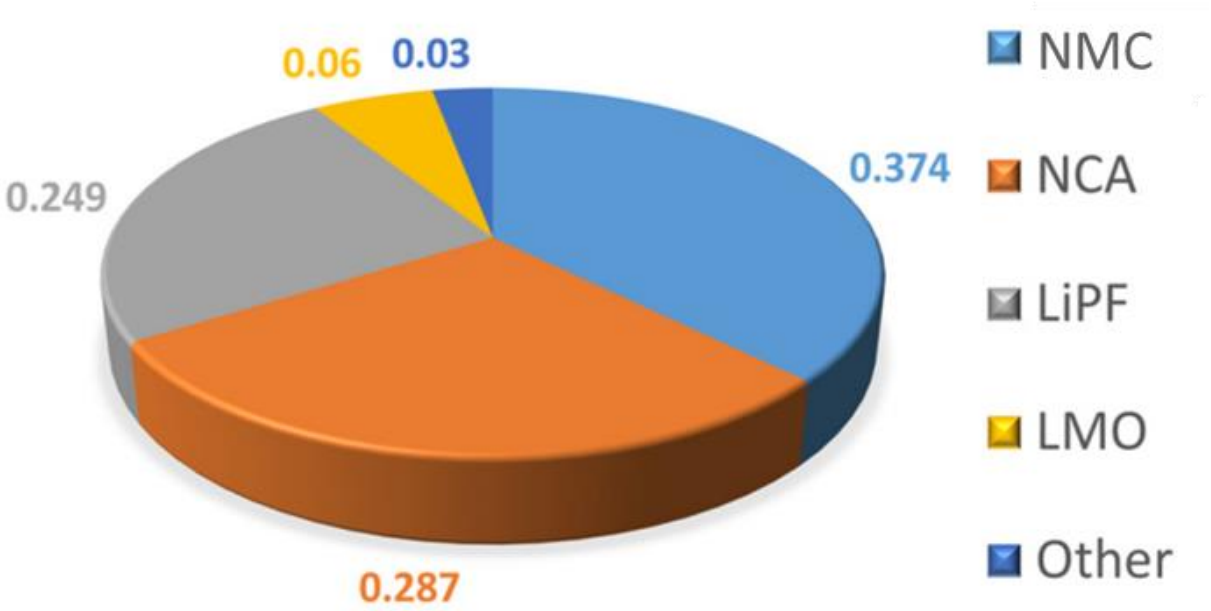

Figure 2-10: Global lithium-ion battery demand by chemistry in 2018 [14]**.**

Figure 2-10 shows the market share for each battery chemistry of lithium-ion technology. The focus will be laid on the three biggest shares. Table 2-1 resembles the comparison of the three biggest chemistries by demand. This chapter will therefore only focus on these chemistries.

Table 2-1: Comparison of lithium-ion chemistries [7]**.**

	lithium iron phosphate	**lithium nickel cobalt aluminium oxide**	**lithium nickel cobalt aluminium oxide**
Chemistry descriptor	LFP	NCA	NMC
specific energy (Wh/kg)	90-120	200-300	150-280
energy density (Wh/l)	190-300	490-675	325
specific power (W/kg)	4000	1000	1000-4000
power density (W/l)	10.000	2000	2000-10.000
Volts (per cell)	3,3 V	3,6 V	3,7 V
cycle life	5000-6000	500	3000-4000
self-discharge (% per month)	< 1 %	2-10 %	1 %
operating temperature range	- 20 °C to + 60 °C	- 20 °C to + 60 °C	20 °C to + 55 °C

Lithium iron phosphate – $LiFePO_4$ – LFP: This cathode is made up of a three-dimensional olivine crystal structured material. The tetrahedral formation of phosphorus, shown in Figure 2-11, bonds tighter with oxygen, making this chemistry safer than others. Furthermore, another material that makes the composition of LFP, iron, is universally available and is a low-cost material. In addition, the use of iron as active material makes the chemistry inherently nontoxic and environmentally safe. However, the biggest downsides of this chemistry are the relatively low nominal voltage as well as a lower energy density, despite the voltage curve being almost straight.

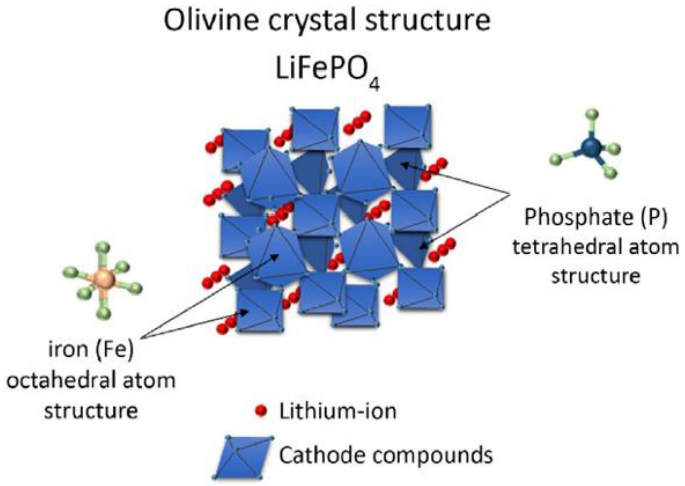

Figure 2-11: $LiFePO_4$ crystal structure [7]**.**

Lithium nickel manganese cobalt oxide – $LiNMnCoO_2$ – NMC: The chemistry of NMC is a combined chemistry of LCO and LCM. It leads to high voltage and a remarkably high energy density. Figure 2-12 shows the crystal structure of NMC. The internal configuration is a pattern of alternating layers. The core of the octagon consists of an oxygen atom. The surrounding atoms depend on each layer and are either a mix of cobalt and nickel or cobalt and manganese. Lithium ions are captivated between the alternating layers. When these different transition metals are combined, the performance is better than when used stand-alone. Some of these benefits are higher discharge capacity, better cycle life, thermal stability, and better rate capacity. Nevertheless, the downside of this chemistry is the high-cost cobalt and no full depth of discharge use for better performance.

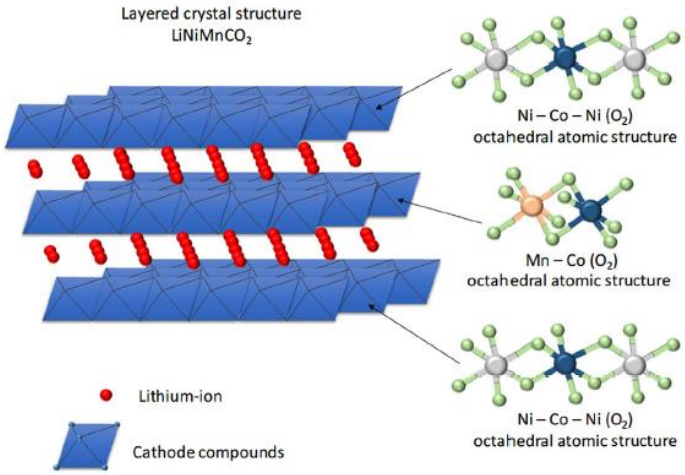

Figure 2-12: Layered structure of NMC [7]**.**

Lithium nickel cobalt aluminium oxide – $LiNiCoAlO_2$ – NCA: Over the last decade, this chemistry has gained a lot of popularity. The market share increased from 10% to 28,7% in three years, from 2015 to 2018, and it has been predicted that it will keep increasing. Furthermore, the structure of NCA is almost the same as that of NMC; the only difference is the use of aluminium instead of manganese. Also, doping the lithium nickel cobalt oxide with the metal stabilizes the thermal and charge transfer resistance. The advantages of this chemistry are high discharge capacity, long storage life and high energy density. On another side, the main downside is the cost, due to the excessive price of cobalt. Another disadvantage of this chemistry is the high capacity fading over time. After a certain amount of cycles, NCA batteries tend to only maintain a capacity of 70% at the maximum [7].

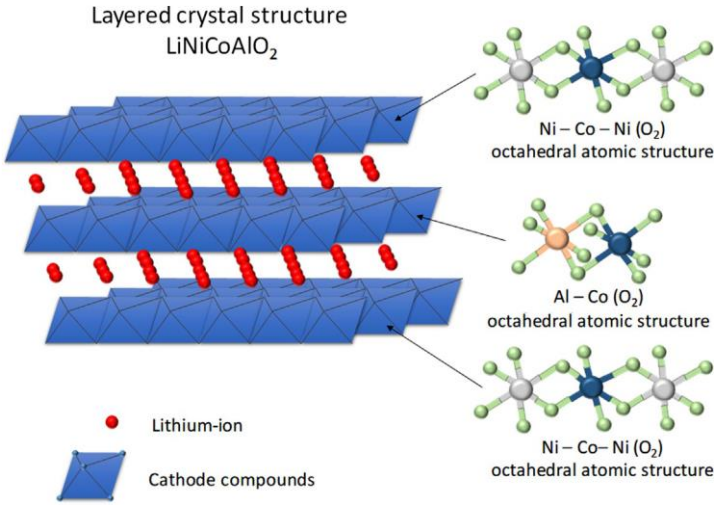

Figure 2-13: Layered atomic structure of NCA [7]**.**

When comparing various lithium-ion cell chemistries, the voltage range is one aspect that must be considered. As seen in Figure 2-14, the range of operating voltages varies for various chemistries.

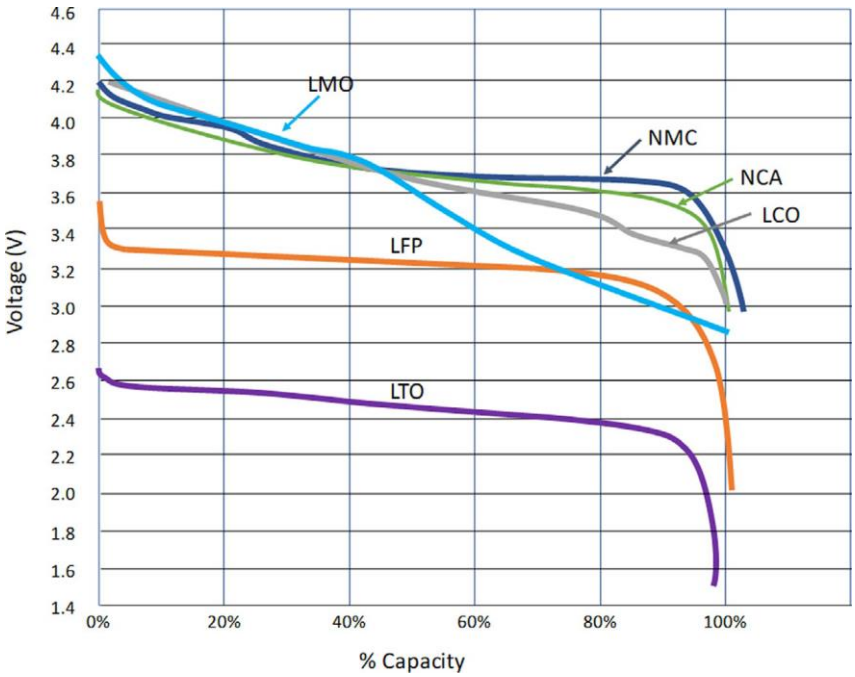

Figure 2-14: Different Li-ion cells and their respective discharge curve [7].

The voltage refers to the difference in electrical potential between the anode and the cathode. This potential difference depends heavily on the specific characteristics of the anode and cathode material, which will in turn affect the resulting voltage in the system. The voltage is an important parameter when designing a battery pack as it determines the number of cells in series to create the defined high voltage. In simpler terms, if the individual cells have a lower voltage, more of them need to be connected in series to accomplish the desired high voltage.

The discharge process starts at higher voltage levels for NMC and NCA chemistries and gradually declines at a consistent rate until the end of discharge voltage is reached. On the other hand, LFP chemistry starts with a lower initial voltage and follows an almost horizontal trend until the end of discharge. Despite these different discharging behaviours, all chemistries show a similar pattern near the end of the curve, which is characterized by a distinct drop-off or “knee” point. The slope of the curves plays a key role when developing the battery management systems control algorithms. If that slope is more flat or constant, it becomes more challenging to determine the precise state of charge based on voltage measurements.

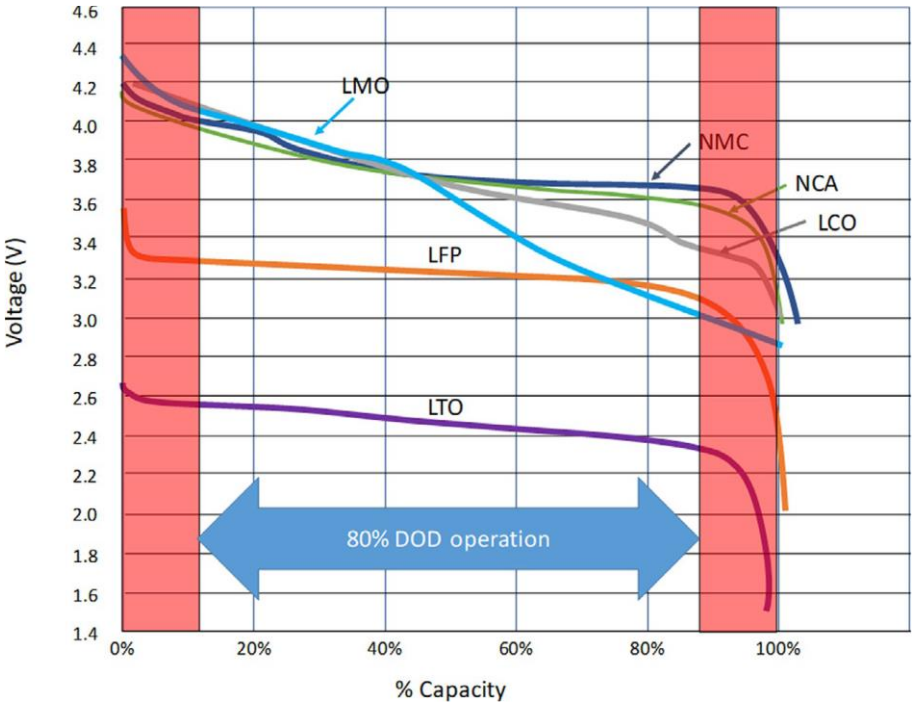

Figure 2-15: Operating voltage range to prevent degradation [7]**.**

On top of that, batteries will never work at 100% DOD. Typically, as a rule of thumb, they only work at 80% DOD by shortening the top and bottom of the voltage span by 10% as in Figure 2-15. The area under the curves in between these boundaries presents now the usable amount of energy of the cells. The first main argument for limiting the voltage range is because for certain chemistries the cathode materials will dissolute in the electrolyte at extreme voltages. This causes premature ageing and reduces cycle life. Another reason to work within a limited voltage range is to compensate for the electronics’ measurement accuracy tolerance. Attempting to fully charge a cell, thus to 100%, can cause severe damage owing to tolerance limits or the earlier mentioned drop-off at the lower end of the voltage curve.

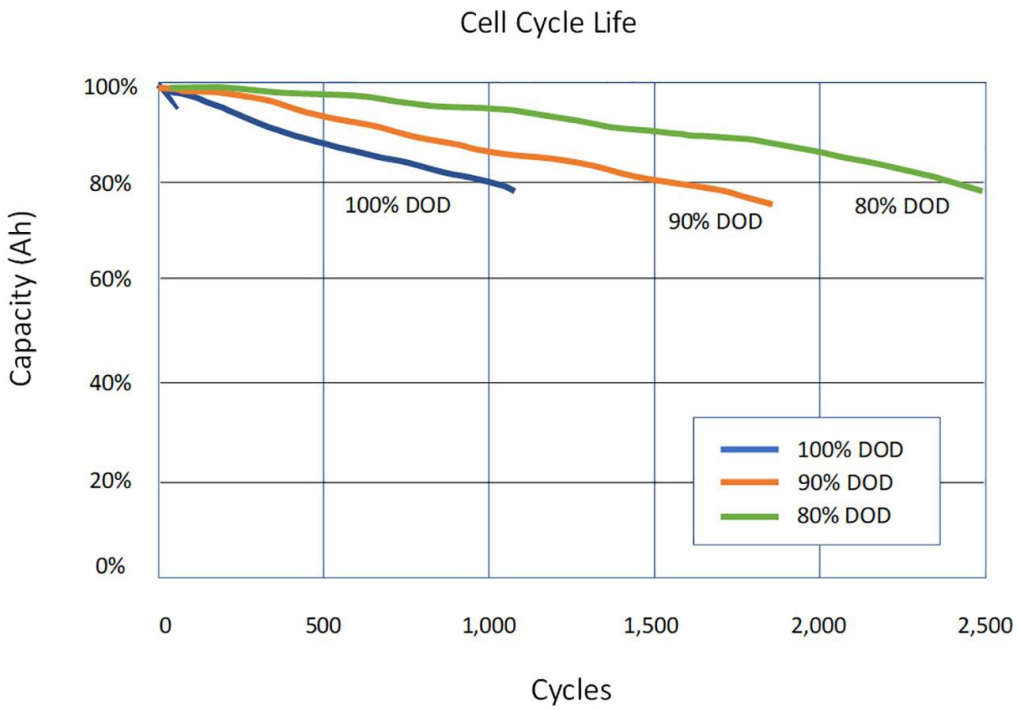

Figure 2-16: Cell cycle life for different DODs [7]**.**

Hence, additional cycles can be gained by reducing the cell voltage operating range. This is graphically shown in Figure 2-16. Another common principle states that for every reduction of 10% DOD, the cycle life is extended by 50% of the original 100% DOD cycle life. To summarise, the first rule of thumb of the 80% DOD means it protects the battery cell and even doubles the cycle life.

2.4.2 Anode electrode chemistries

Typically, carbonaceous materials make up anode electrodes. The material must have strong chemical and electrochemical stability with the electrolyte and be able to hold substantial amounts of lithium without significantly altering its structure. Additionally, it should be relatively inexpensive and a good electrical and ionic conductor. The major material for the anode is graphite. This material can either be made or mined, representing respectively synthetic or natural graphite. Silicon is considered a potential future alternative to graphite as an active anode material.

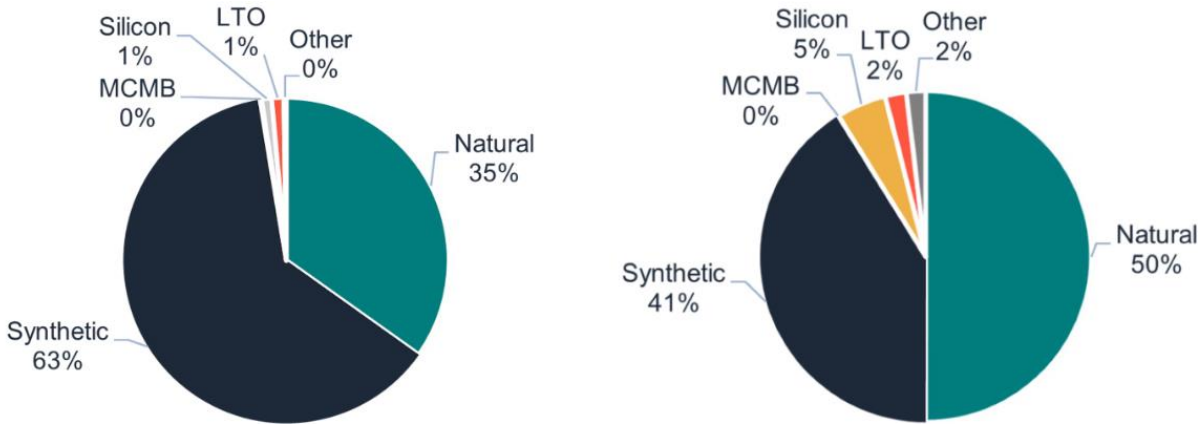

Figure 2-17: left: 2022 Composition of Active Anode Material for Batteries; right: 2030 Composition of Active Anode Material for Batteries [15]**.**

Graphite: A highly favourable material for the anode is graphite. The reason being graphite is inexpensive and abundantly available. In addition, the processing of the material is very straightforward. The reversibility during the inter- and deintercalation processes is effectively high. This translates to an efficient insertion and removal of lithium ions during charging and discharging cycles, without significant degradation or loss of performance. Moreover, the voltage potential is almost zero compared to lithium, which is a key factor for the stability of the SEI layer upon formation.

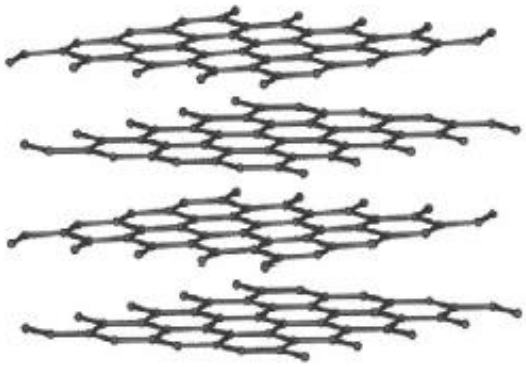

Figure 2-18: Graphite structure [7]**.**

The structure, shown in Figure 2-18, is a graphite structure. It represents the repeating layer of carbon atoms bonded in a hexagonal-shaped formation. A lithium-ion fits in the hexagon of carbon atoms.

All the above advantages make graphite the most popular anode material in lithium-ion cells. It offers stability, efficiency, affordability, and reliability.

Additionally, battery-grade graphite falls into one of two classes: natural or synthetic. The difference between the two lies in the production process.

Natural graphite is mined. During the spheroidization process, flake graphite particles are mechanically rounded. This leads to the loss of some material but yields improvements in the performance of the anode. Currently, China provides around 70% of all-natural graphite [16].

Synthetic graphite on the other hand is not mined. It is produced by high-temperature treatment of carbon precursors such as petroleum coke, coal tar pitch, or carbon black. The graphitisation of coke products into synthetic graphite requires the largest energy input. If fossil-based electricity is used for this process, then the carbon emissions increase substantially. The production of synthetic graphite is over four times more pollutant than the mining of natural graphite. With the focus on sustainability, the market share of synthetic graphite will drop naturally over the next years.

Silicon: In comparison to graphite, silicon has a higher theoretical energy and volumetric density, which translates to a higher capacity and could enable faster charging. To take advantage of these benefits, silicon is currently employed in battery anodes in tiny amounts, up to 5% by mass. However, when silicon is used in greater quantities in a battery anode, it swells significantly more than graphite during charge/discharge cycling, leading to cell instability, capacity degradation, and decreased cycle life. These crucial problems have not yet been resolved technologically, which is necessary for silicon to be applied in the real world as a scale-up substitute for graphite. Future anode product development continues to focus on blending silicon and graphite [7], [15].

2.4.3 Electrolyte

The electrolyte, an ionically conducting medium, is essential for the movement of lithium ions between the cathode and anode in an electrochemical cell. It plays a crucial role to ease the transfer of ions back and forth. In essence, the medium serves as a pathway for the lithium ions to travel between the two electrodes, enabling the proper functioning of the cell [7].

The focus of research is progressively shifting toward electrolytes since they have an impact on a battery's current (power) density, time stability, reliability, and ability to construct solid electrolyte interfaces. Solid and liquid electrolytes are both available. Figure 2-19 illustrates only a few of the countless permutations of these two fundamental groups of electrolytes. Liquid electrolytes are either aqueous or non-aqueous. There exist three different types of aqueous electrolytes: acid, alkaline or neutral. For non-aqueous electrolytes, ionic electrolytes are distinguished from organic ones. Solid-state electrolytes can be sorted by their polymer as dry solid, gel or inorganic. [17].

Lithium-ion battery performance and safety both depend heavily on the electrolyte selection. Usually, an organic solvent combination containing lithium salt serves as the electrolyte. A good electrolyte should ensure efficient battery operation and safety through qualities such as a big range of electrochemical voltage stability, high ionic conductivity, low toxicity, a w reactivity with other cell components, and good thermal stability [2].

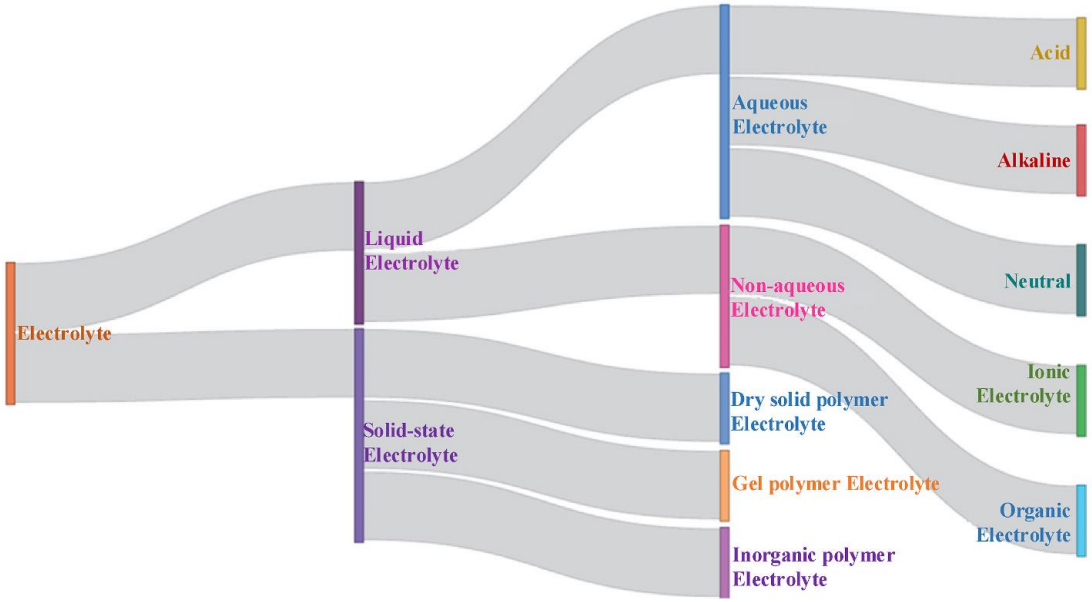

Figure 2-19: Sankey diagram for electrolyte materials [17]**.**

A lithium-ion electrolyte is a solution, most often liquid, of organic solvents mixed with a solute made up of lithium salts and other additives. Most of the electrolytes used in commercial lithium-ion batteries are non-aqueous solutions. Such as Lithium hexafluorophosphate (LiPF6) salt dissolved in organic carbonates, which is the most commonly used in lithium-ion [18].

Other options are explained underneath:

NASICON is an acronym for natrium super ionic conductor. It is a solid electrolyte known for its high ionic conductivity [19].

Garnet electrolyte refers to a class of solid-state electrolytes that use a garnet crystal structure as the host material [20].

Polymer electrolytes are polymer matrices capable of ion conduction. There exist four major types of polymer electrolytes: gel, solid-state, plasticized and composite [21].

Sulphide solid electrolytes are derived from oxide solid electrolytes. The oxygen ions are swapped with sulphur ions to enhance the ionic conductivity and improve performance [22].

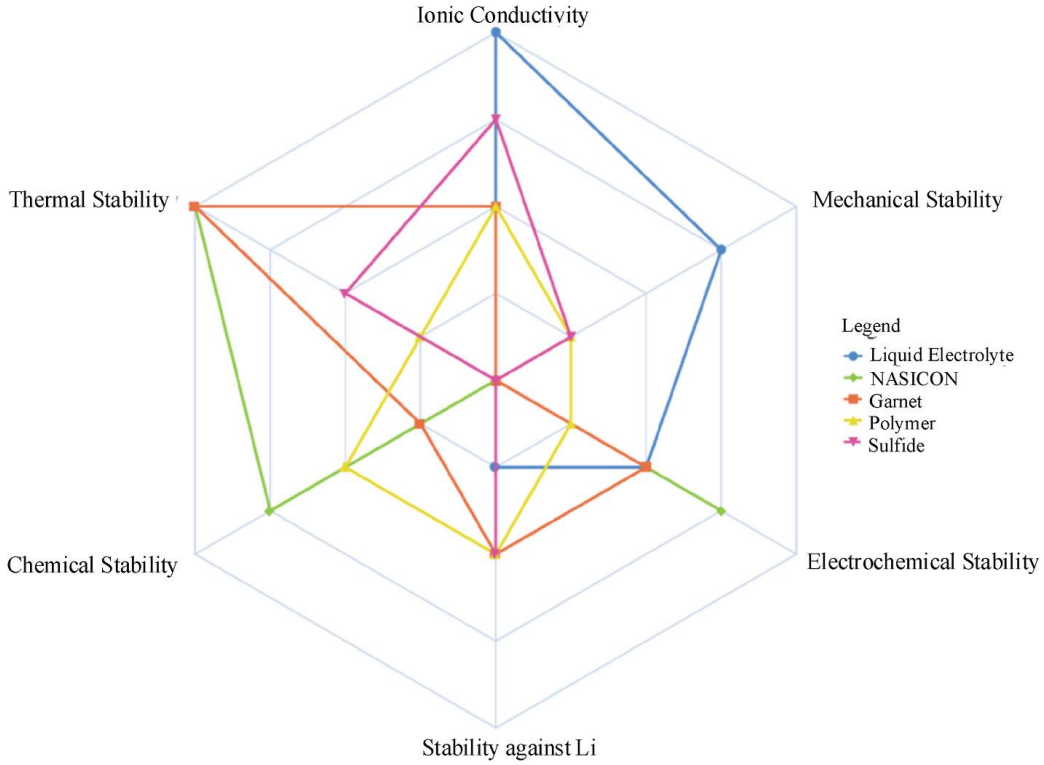

Figure 2-20: Different electrolytes and their qualities [17]**.**

According to the radar map portrayed in Figure 2-20, different materials have variable degrees of stability. For example, Garnet and NASICON are thermally most stable, however, NASICON also stands out regarding chemical stability despite being less stable than lithium. Moreover, the ionic conductivity of NASICON is better compared to other electrolytes. Overall, it appears that NASICON is the most steady electrolyte substance [17].

2.4.4 Separator materials

The separator plays a crucial role in physically separating the electrodes from each other while still allowing ion flow. There exist several choices for a separator, each offering different properties.

The first type is the nonwoven. The separator material is composed of fibres arranged in a random directional manner. Another type is the supported liquid membrane which is a composition of both a liquid and a solid phase. Polymer separators, which are a solid type of separator, form complexes with alkali metal salts to create solid ion conductors. This solid type can function as both separator and electrolyte.

When the battery is fully charged and exposed to highly reactive environments, the separator must exhibit chemical stability against the electrolyte and electrode materials. A thin separator is desirable, but it still should possess sufficient tensile strength to avoid damage or stretching during the winding process.

The porosity is also important, for example, it is harder to close the pores during a battery shutdown situation when the porosity is large. But a too small porosity will make the battery slow. Typically, the porosity should be about 40% [23]. The pores should be uniformly distributed and ensure uniform current distribution throughout the separator.

In addition, the separator must not show significant degradation under normal operating conditions. To guard the thermal stability, the separator needs to switch off when the temperature reaches a certain upper limit to prevent thermal runaway from happening.

Lastly, compatibility with the electrolyte must ensure complete wetting protecting the cycle life. It surely is challenging to achieve these properties in a single separator, but it is necessary to ensure reliability, performance and efficiency [24]–[26].

2.4.5 Current collectors

Other essential components in lithium-ion cells are current collectors. They bridge the gap between the electrodes and the external circuit for electrical current to flow. Aluminium and copper foils are among the most commonly used materials for the cathode and anode respectively [27].

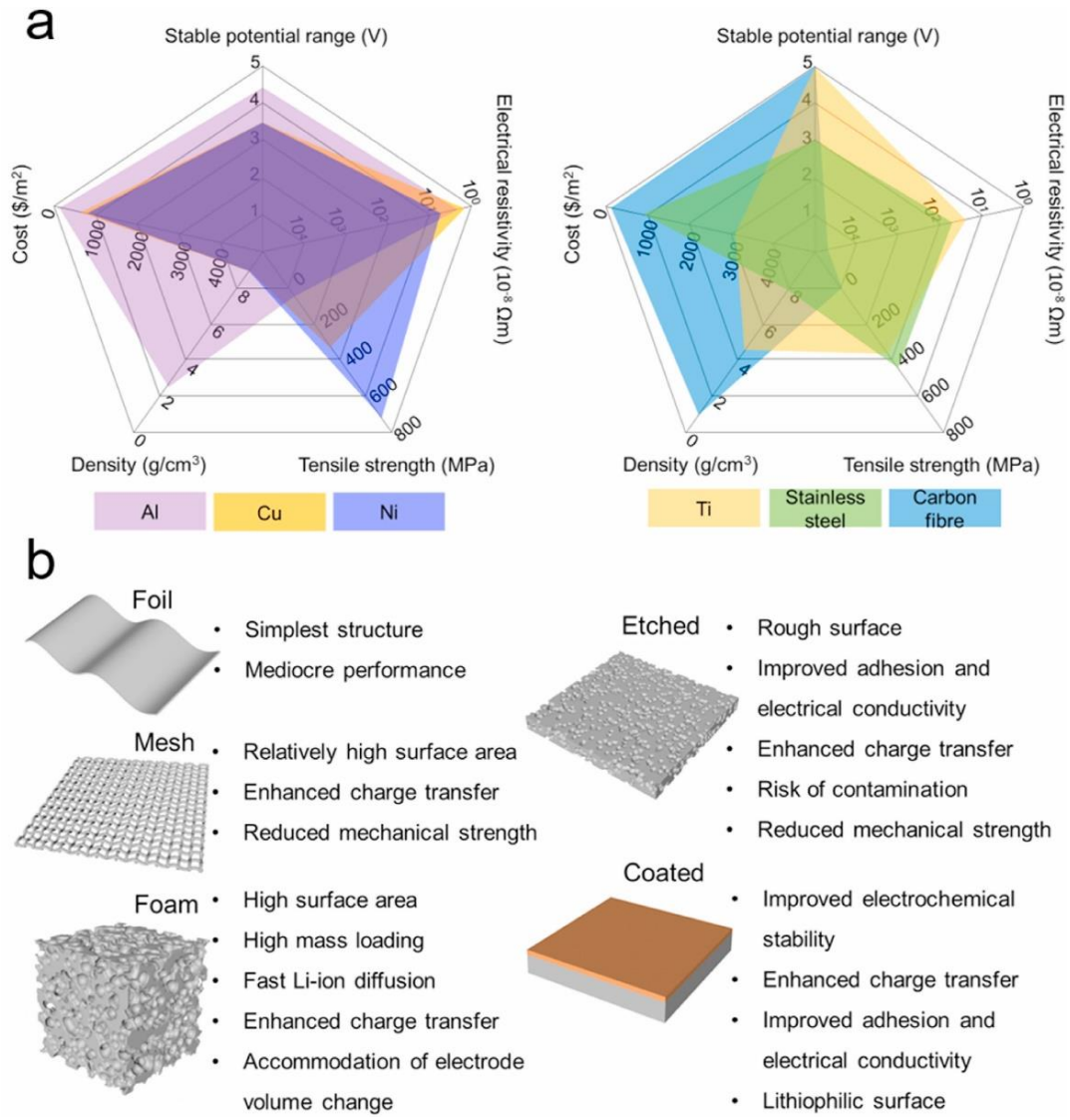

Figure 2-21: a) A comparison of different current collector materials; b) The pros and cons of various current collector structures [28]**.**

The performance of various materials as current collectors for cathodes and anodes in lithium-ion batteries is covered in Figure 2-21a. The voltage range stability, electrical resistivity, tensile strength, density, and cost of the materials are contrasted. As carbon fibre paper has the lowest density, it is suggested to be a good option for current collectors. However, the largest stable potential range is found in titanium and carbon fibre, whereas copper has the lowest resistivity. Aluminium and copper foils can be easily separated and recycled, while nickel has the maximum tensile strength. The pricing and sustainability of the materials vary widely, with carbon being the most accessible and least priced while titanium is the most expensive [28].

Figure 2-21b discusses the pros and cons of structures and treatments applied to current collectors. The simplest current collector is foil; however, its performance is average compared to other forms of current collectors. Mesh current collectors have lower mechanical strength but a better surface area and charge transfer kinetics. Foam current collectors exhibit a larger surface area, efficient Li-ion diffusion, and can accommodate electrode volume change during cycling. The loading method is crucial for foam and mesh current collectors. On the other side, chemical etching reduces mechanical strength and increases the danger of contamination, while roughening the surface of current collectors to increase adhesion and interfacial conductivity. Furthermore, the coating can increase charge transfer efficiency, electrochemical stability, and dendrite development. By guiding homogenous Li nucleation and deposition with lithophilic coatings, dendrite formation can be potentially prevented [28], [29].

2.5 Battery cell design

Several configurations exist to design a battery cell. The design choice depends mostly on the application. Figure 2-22 presents the most popular battery designs.

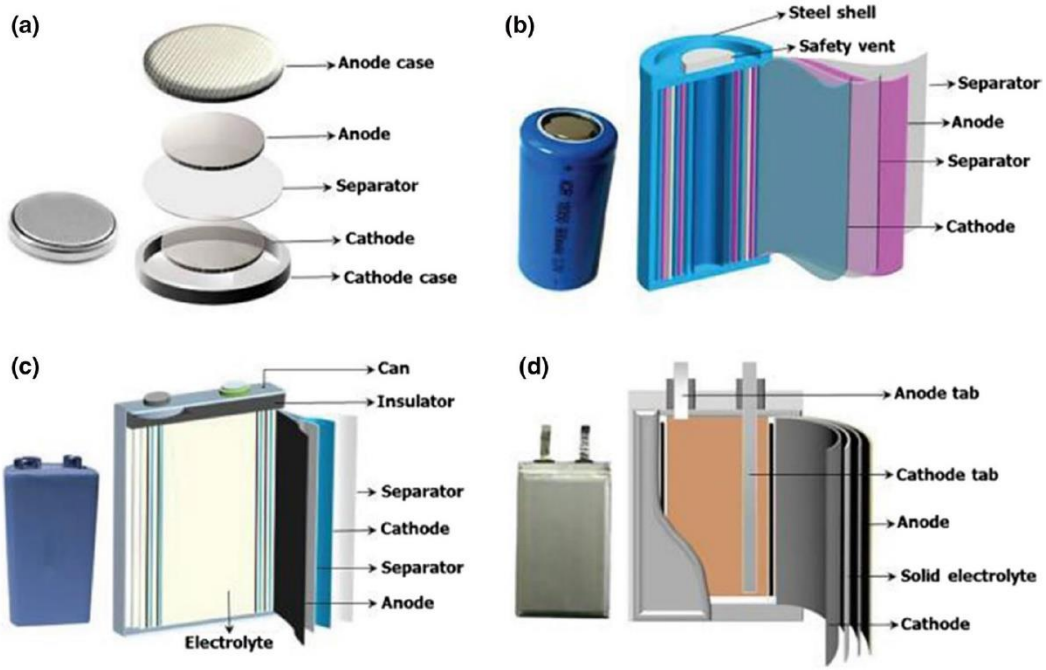

Figure 2-22: Various battery types; a) Coin cell; b) cylindrical jelly-roll; c) Prismatic cell; d) Pouch cell [30]**.**

Coin, cylindrical, prismatic, and pouch lithium-ion batteries are the most prevalent commercial types in use today. Cylindrical cells often have a standard model size, for example, 18650 cell models are found in many EVs [31]. In comparison to prismatic and pouch cells, cylindrical cell batteries usually exhibit a higher volumetric energy density during an assembly at high tension. Furthermore, cylindrical cells can provide higher power which makes them suitable for high-performance applications [32], [33]. Prismatic and pouch cells are more frequently utilized despite cylindrical cells having better energy densities than them. Their lower dead volumes at the module level and the better design flexibility make these cells more adaptable to specific products, which cylindrical cells lack [34].

2.6 Battery pack design

A battery pack is an arrangement of multiple cells connected in series, in parallel or combined. This configuration allows for the pack to deliver both the high voltage and the high capacity of a particular application. Figure 2-23 illustrates all arrangements for the design of a battery pack. Usually, the configuration is named according to the amount 'n' of cells in series 's' and the number of cells 'm' in parallel 'p', which gives the configuration 'nsmp'. For example, a 24s5p pack contains 24 cells in series and 5 in parallel [35].

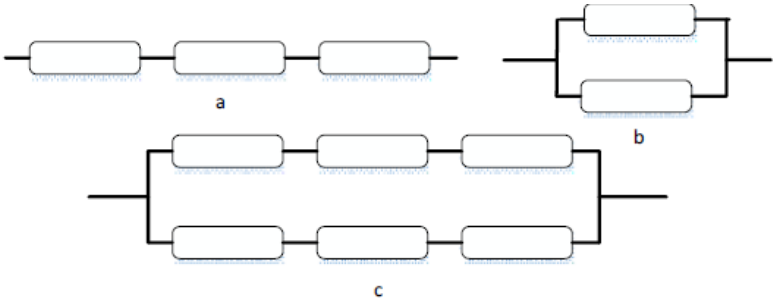

Figure 2-23: All battery pack configurations: a) series connection, b) parallel connection, c) series-parallel combination [35]**.**

A battery with parallel connections is created by connecting multiple cells side by side, with their terminals connected accordingly. When cells are connected in parallel, current is simultaneously fed and drawn, into and from each cell, respectively. The system capacity increases while the overall voltage remains constant. The three cells in the example below are each assumed to be 3.6 V and 5 Ah; if they were connected in parallel, the voltage would remain at 3.6 V but the capacity would increase to 15 Ah (5 Ah x 3 cells) [27].

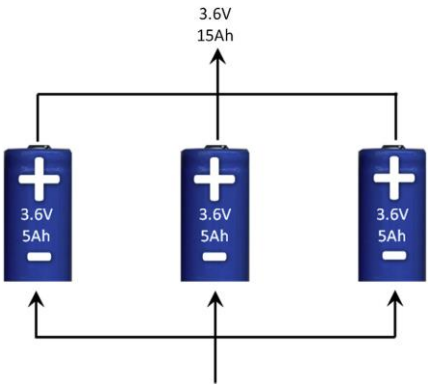

Figure 2-24: Parallel cells [27]**.**

On the other hand, a series configuration involves connecting several cells "chain wise", the positive terminal of one cell is connected to the negative one of the other. The voltage of the entire system is increased by connecting cells in series. The example below in Figure 2-25 illustrates three cells, which we'll assume are in a series configuration and have the same specifications as our previous example—3.6 V and 5 Ah. This setup would produce 10.8 V (3.6 V multiplied by 3 cells), but the output capacity would stay at 5 Ah [27].

Figure 2-25: Lithium-ion cell in series connection [27]**.**

2.7 Temperature effect and thermal impact on lithium-ion batteries

Temperature is a critical factor for the performance and efficiency of lithium-ion batteries, which in turn can limit potential applications. Several temperature conditions may have varying adverse effects on these cells. Despite their high energy and power density, temperature-related issues still constrain these batteries. Typically, the operating temperature range is between -20 °C and 60 °C, in which the cell operates optimally between 15 °C and 35 °C [36], [37]. When temperature either exceeds the lower or the upper limit of this range, a decline in performance can occur with the possibility of irreversible damage like lithium plating and thermal runaway [38]. Therefore, it is essential to understand the influence of temperature as well as how to accurately measure the temperature inside the cell to manage it properly [39].

2.7.1 Low-temperature effects

The performance and safety of batteries are significantly impacted by extended exposure to low temperatures. When subjected to cold temperatures, the electrolyte's viscosity increases, leading to a decreased ionic conductivity. Subsequently, the internal resistance rises according to the impedance encountered by the migrating ions. In other words, the battery requires more energy to charge, resulting in lower capacity [38], [39]. The charge-transfer resistance significantly increases when temperature decreases, affecting the kinetics in batteries. Lithium ions diffuse slower within the electrodes, which deteriorates the cell performance [40], [41]. At lower temperatures, the chance of lithium plating increases [42]–[44]. The cold environment activates anode polarization, causing the potential of the anode to almost equal that of lithium metal [45]. This slows down the intercalation of lithium ions into the anodes. Henceforth, the lithium ions accumulate on the electrode surfaces, leading to a reduction in battery capacity. Moreover, extreme accumulation can cause dendrites to penetrate the separator leading to internal short-circuit [39].

2.7.2 High temperature effects

Where low temperatures are a result of the environment, elevated temperatures can also be caused by internal heat generation within the battery cell. Figure 2-26 shows that heat is either generated during a reversible or irreversible process [46]–[48]. Reversible heat is generated during the reversible change in entropy that occurs during electrochemistry [49]. Meanwhile, irreversible heat is generated through various processes. As a result of the overpotential between the operating potential and the open circuit potential of the batteries, active polarization leads to the increase of charge transfer resistance at the solid electrolyte interface. Heat is produced when lithium ions overcome such resistance at the interface for their (de)intercalation [50]. Ohmic heat is the result of the resistance encountered by electrodes and electrolytes when transporting charges [51], [52]. During (dis)charging, the ion distribution becomes inhomogeneous which leads to the mixing of ions, this generates heat [46], [53]. Furthermore, while lithium ions diffuse in cathodes, a phase change can occur, resulting in an enthalpy change and subsequent heat generation [54].

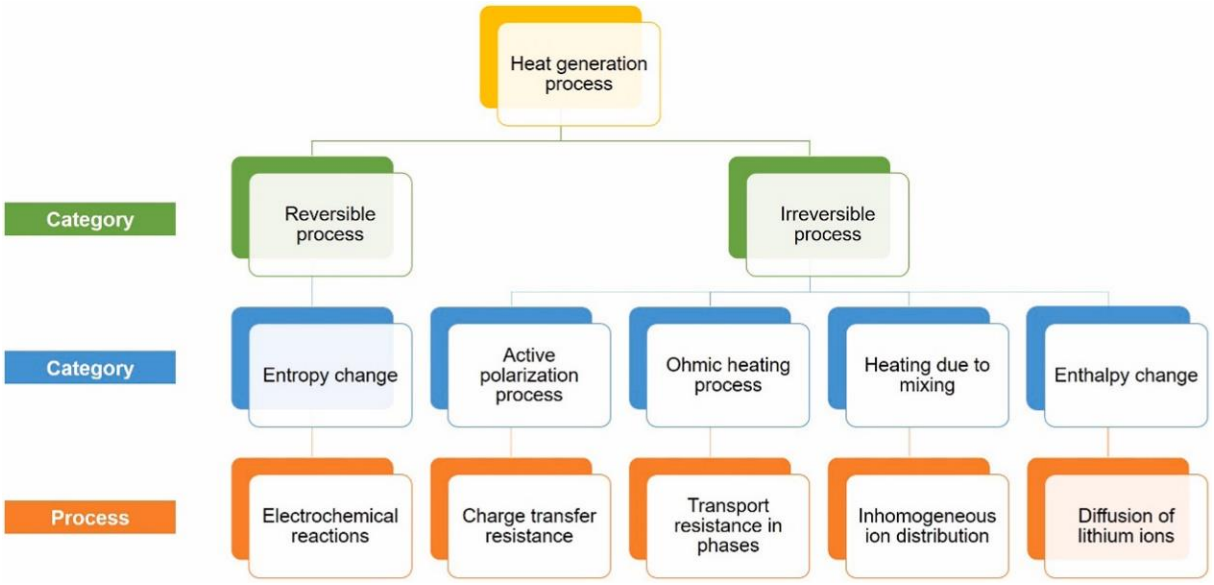

Figure 2-26: Different sources of heat generation within LIBs [39]**.**

2.7.3 Thermal runaway

Two main causes stand in for the occurrence of thermal runaway. Either the battery is not manufactured properly and comes with certain defects, or the cell is used incorrectly. Hot temperatures cause exothermic reactions within the cell, which in turn release even more heat. Consequently, the temperature further increases over a certain point, at which it continues to grow on its own. Furthermore, when this process becomes self-sustaining and generates oxygen to fuel the fire, thermal runaway occurs. Even worse, when the heat exceeds the battery's capacity to withstand it, fire and explosion will occur. Figure 2-27 gives the possible steps before reaching a thermal runaway [7], [55], [56].

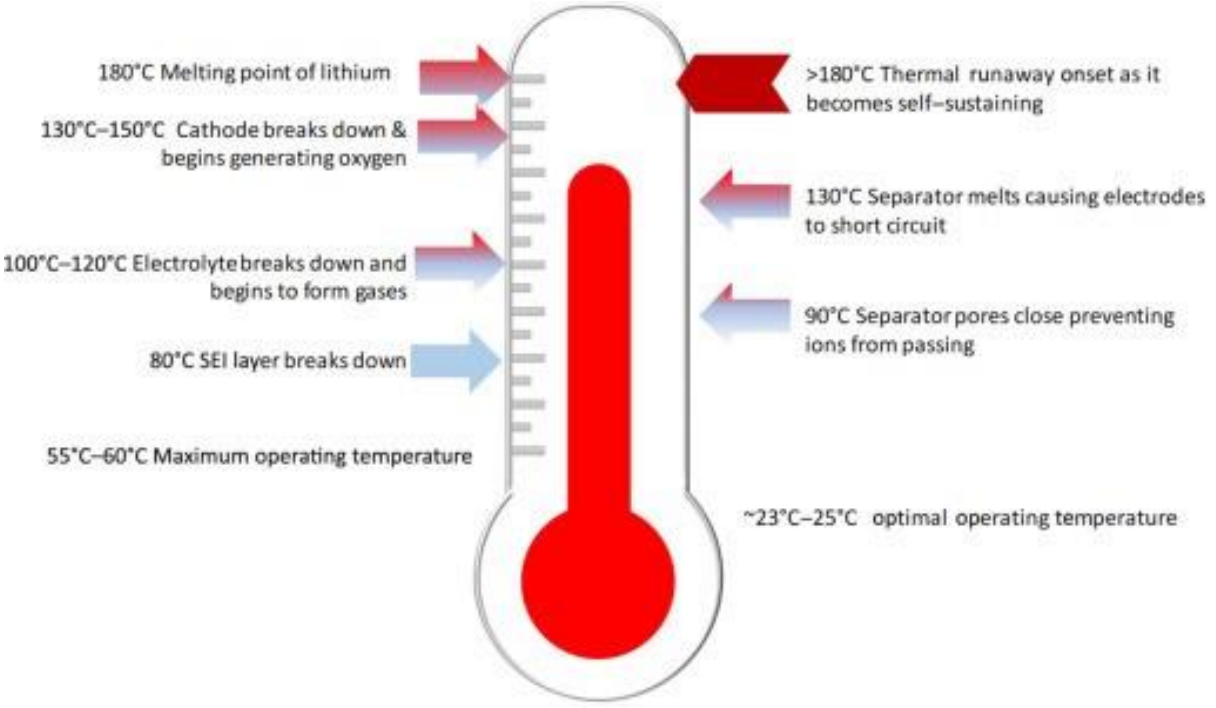

Figure 2-27: An example of temperature levels eventually leading to thermal runaway [7], [55], [56]

2.8 Effect of thickness of components

2.8.1 Electrode thickness effects

Research shows that the rate capabilities of lithium-ion batteries reduce when the electrode thickness increases [57]. The thicker electrode can however improve the energy density of the battery cell but also raises internal resistance. Hence, the power density and rate capability decrease. Since ohmic heat is proportional to the resistance, more heat is generated which limits the transport capacity of the electrolyte [57].

When the electrode thickness increases, the ability to discharge at high currents or C-rates decreases. Furthermore, at 50% SOC, the power density during pulse discharge also acts inversely proportional to the discharge and internal resistance. Cells with thinner electrodes tend to experience less capacity fading over time, however, the internal resistance of the cell increases with each cycle [58].

Additionally, increasing the thickness of the electrode in a $LiFePO_4$ also increases the electrode impedance, thus decreasing the conduction rate of lithium ions in the electrolyte [59].

In Figure 2-28, the relationship between the electrode thickness and the energy density is plotted for both per weight and per volume, in red and blue respectively. A thicker electrode leads to a better energy density of the cell. Nevertheless, it is worth mentioning that the magnitude of this effect gradually decreases with increasing electrode thickness.

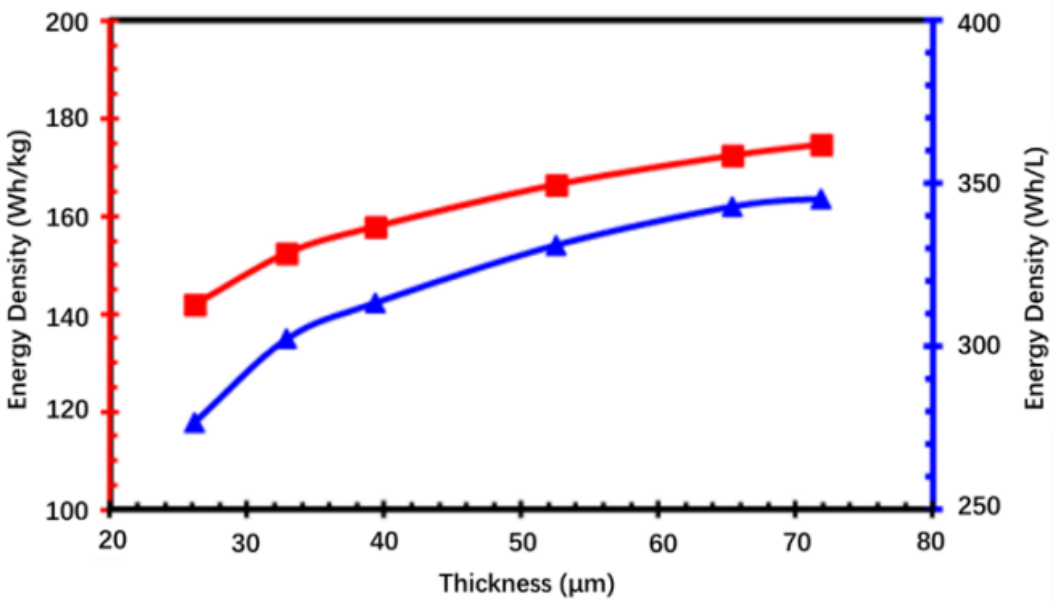

Figure 2-28: Relationship between electrode thickness and energy density [58]

The structure of the electrode impacts the discharge ability of the cell. When the discharge ratio is low, the active layer of the electrode is smaller than the characteristic diffusion length of the lithium-ion. First, the correlation between the discharge rate and the characteristic diffusion length is proportional. The electrode is enabled to release all its designed capacity when the characteristic diffusion length equals the thickness of the electrode. In turn, this results in a further increase in the discharge rate. Now the characteristic diffusion length reduces, and the discharge capacity dives under the design capacity [60].

In Figure 2-29a, the positive electrode of the cell has a thickness of 26,2 µm. For the 20 C condition, the cell can release nearly all its designed capacity. In Figure 2-29b, tests are conducted for an electrode with a thickness of 71,8 µm. Over 3 C the cell fails to release the designed capacity and to completely release all the lithium ions from the active particles. Noticeable is the sharp drop when the C-rate surpasses a certain threshold. In Figure 2-29b, the internal polarization of the cell leads to this sharp drop under 7C conditions. For high lithium-ion concentration differences in the active zone, while discharging, the solid-state diffusion of the lithium-ion acts as the limiting factor. As a consequence, the potential of the electrode immediately drops to the cut-off voltage [61], [62].

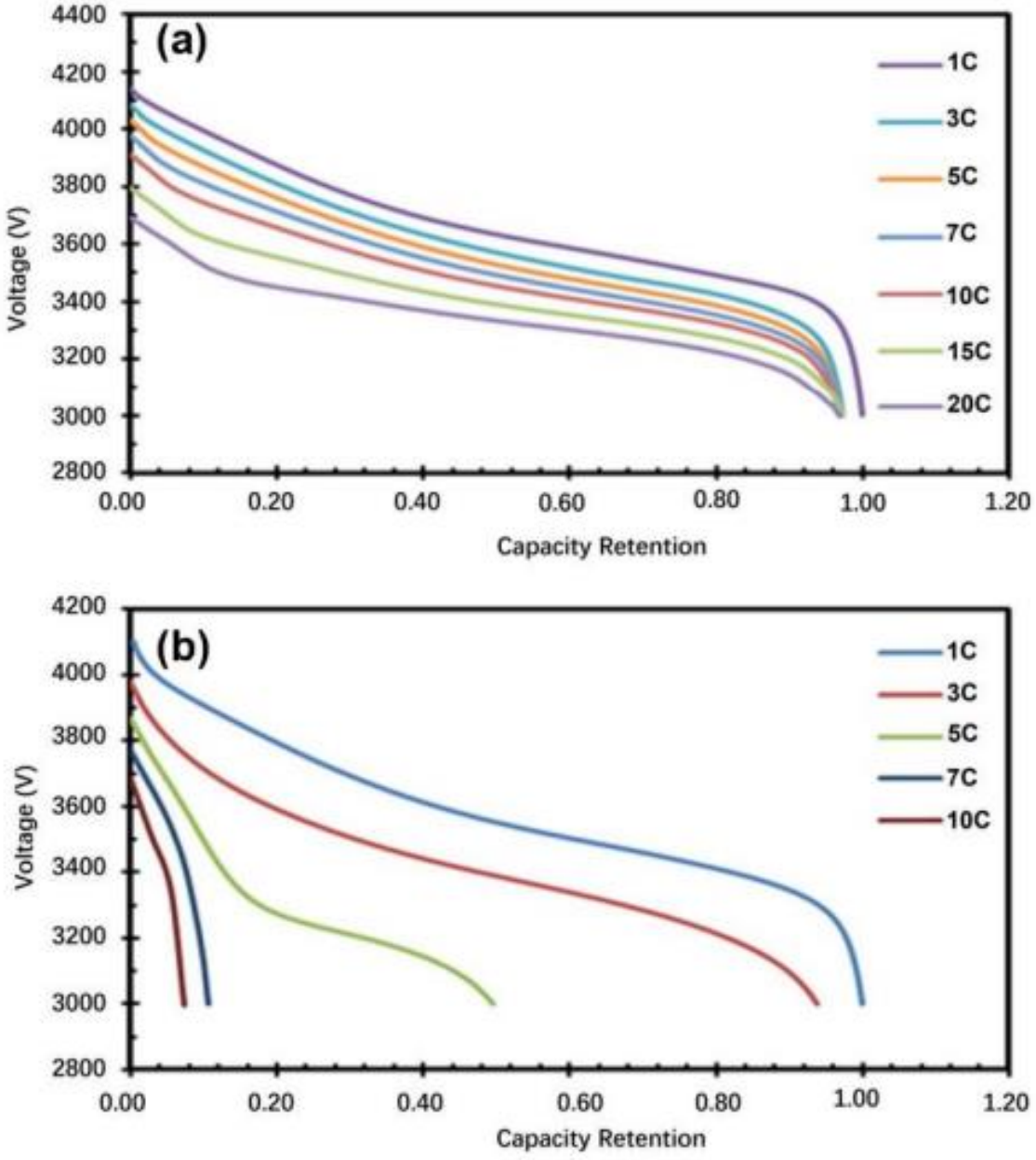

Figure 2-29: Discharging under different conditions for (a) 26,2 µm electrode thickness and; (b)71,8 µm electrode thickness [58]**.**

2.8.2 Separator thickness effects

To maximise the energy density, the component that doesn't contribute towards energy storage needs to be minimized. This requires the separator volume to be minimised while retaining its core functionality, thus reducing the separator thickness. As a consequence, the resistance of the electrolyte within the separator decreases, which in turn reduces the time associated with the diffusion of ions across the separator [63], [64].

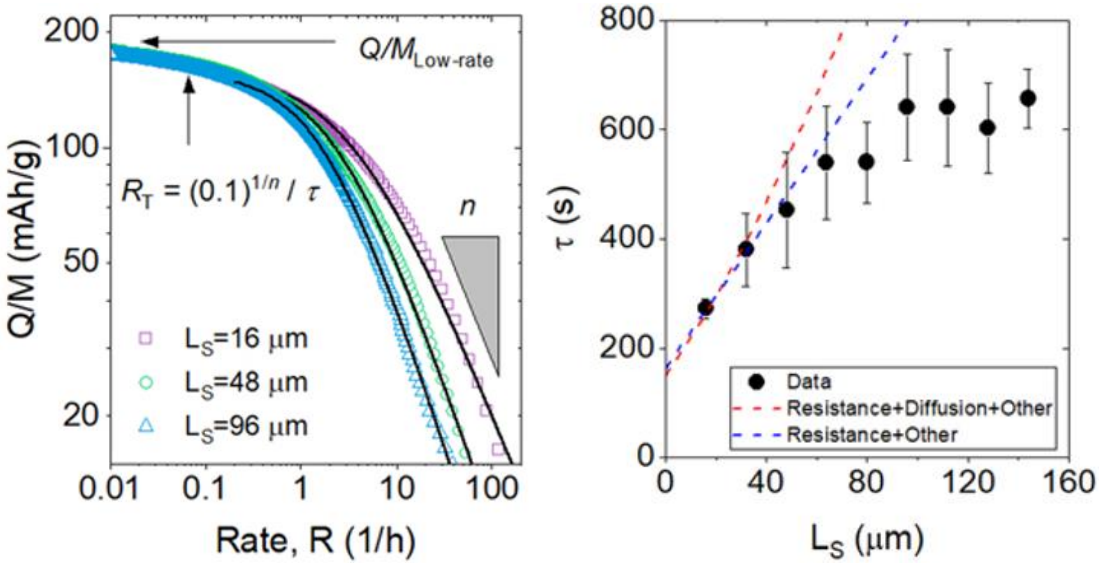

Figure 2-30: Quantifying the effects of separator thickness (L_s) on rate performance; left: Specific capacity (Q/M) vs rate I curve for three different separator thicknesses as acquired from chronoamperometry; right: characteristic time τ as a function of L_s [65]**.**

Figure 2-30 clearly shows that cells with thinner separators display higher specific capacity at higher rates. This confirms the earlier statements. Also, the characteristic time appears to increase linearly with separator thickness, before saturating at thicknesses above ~100 μm. According to this analysis, ion diffusion inside the separator is a far less significant rate-limiting factor than the resistance of the electrolyte inside the separator [65].

2.8.3 Current collector thickness effects

The main focus to enhance the specific energy of lithium-ion cells is to develop advanced electrode materials with high capacity and boost the amount and density of active materials within the batteries [66]–[69]. Even though this leads to higher specific energy levels, a major drawback is the increase of "dead weight" contributed by the current collectors. Therefore, there's a lot of potential to further increase the energy density by making the current collectors lighter [70].

The prime aim to increase the specific energy of batteries is to develop new high-capacity electrode materials and increase active material loading and density [66]–[69]. This has led to higher specific energy, but the percentage of "dead weight" from metal current collectors (Cu for anodes and Al for cathodes) has increased as well. Hence, there's a lot of potential to further increase the energy density by making the current collectors lighter [70].

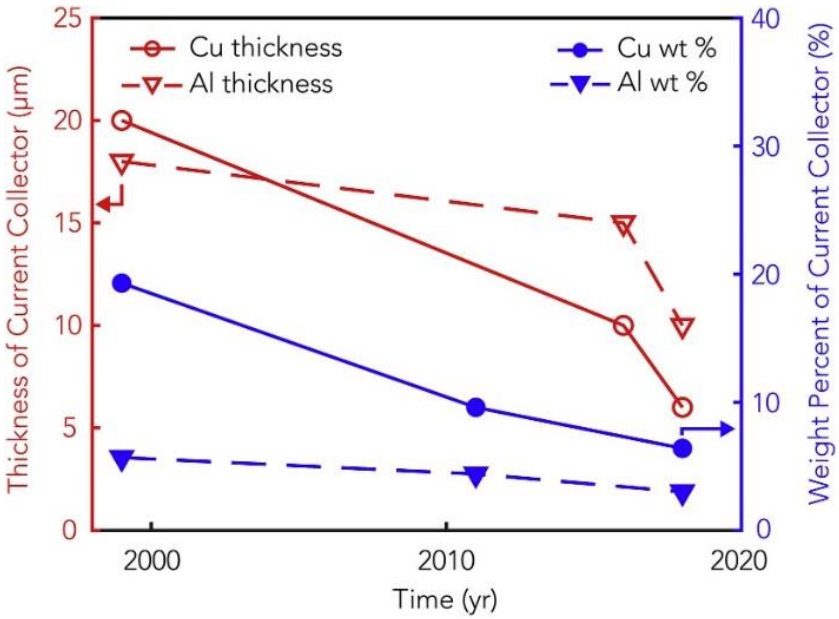

Figure 2-31: Current collectors' trends over the last two decades [70]**.**

Figure 2-31 illustrates the development of the current collector's dimensions over the past years. According to the latest advancements, the current collector's thickness and weight percentage are respectively 6 µm or 6,4% for Cu and 10 µm or 3% for Al [71].

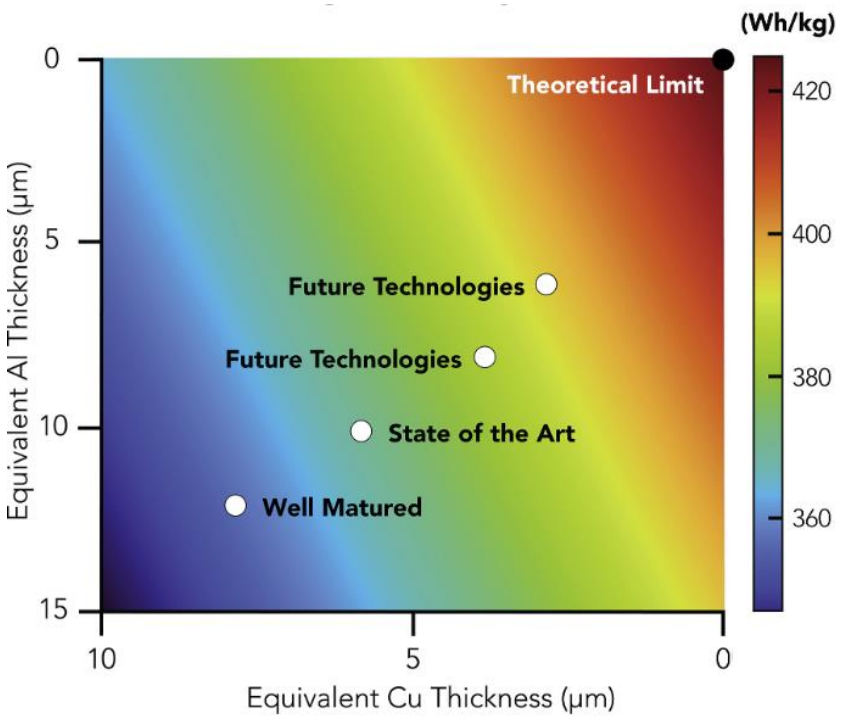

Figure 2-32: Impact of current collector thickness on specific energy [70]**.**

Furthermore, Figure 2-32 shows the future possibilities for enhancing the specific energy of batteries. The graph shows that the specific energy relies more on the thickness of copper than aluminium due to its higher energy density. By reducing the weight of the current collectors an increase in the specific energy is forecasted to be 5 % to 20 % [70].

3 CFD PARAMETRIC STUDY OF CELL COMPOSITION

This chapter describes all the practical work done within the scope of this dissertation. First, the theoretical derivation of the equivalent material properties of one cell and the reason behind it is explained. Then, a CFD model and electrochemical submodel are chosen for simulation. Further, a design of experiments is set up and explained in detail.

3.1 Battery properties

The datasheet of the LiFePO4-32700- 6 Ah cylindrical rechargeable lithium-ion cell is attached in appendix A. As earlier described, the main goal of this work is to find a method to determine the inner configuration of this cell. The main applications of this cell are EVs and PHEVs, UPS and telecom, energy storage or starting power supply. The benefits of this LFP battery described by the company are [72]:

- *"Sturdy and pressure-resistant steel envelope*
- *High capacity*
- *Excellent cycling life*
- *Excellent high and low temperature performance*
- *Steady output voltage*
- *Low self-discharge*
- *Double safety protection*
- *Outstanding high level against vibrations and shocks*"

Important specifications of the cell are given in Table 3-1 underneath:

Table 3-1: LiFePO4-32700- 6 Ah nominal specifications [72]**.**

Item	Specification
Nominal Capacity	6 Ah
Nominal Voltage	3,2 V
Cell Diameter	32,2 ± 0,3 mm
Cell Height	70,5 ± 0,3 mm
End-of-charge Voltage	3,65 V
End-of-discharge Voltage	2,00 V

3.2 Equivalent material properties

In the CFD software Ansys fluent, it is not possible to give the battery cell its inner spiral configuration of several component layers such as current collectors, electrodes, and separator. However, if this was possible, it would not be optimal as it would greatly increase the calculation time. That is why the battery is modelled as a black box, therefore it is important to calculate the equivalent material properties of the entire battery cell. To achieve this, a new model is developed and validated with data from external sources.

3.2.1 Simplification of the internal configuration

The internal configuration of the cell, displayed in Figure 3-1, is a spirally wound jelly roll where one 'cell layer' (defined in the right part of the figure) consists of five sheets of material: the positive current collector, the positive electrode, the separator, the negative electrode, and the negative current collector. These sheets are very thin, which makes it possible to approach it as a layered structure in which each layer has a constant radius from the centre point. The battery cell is represented in such a way in the upper left corner of Figure 3-2. This prevents including the angle of the spiral in the calculation, which simplifies the arithmetic.

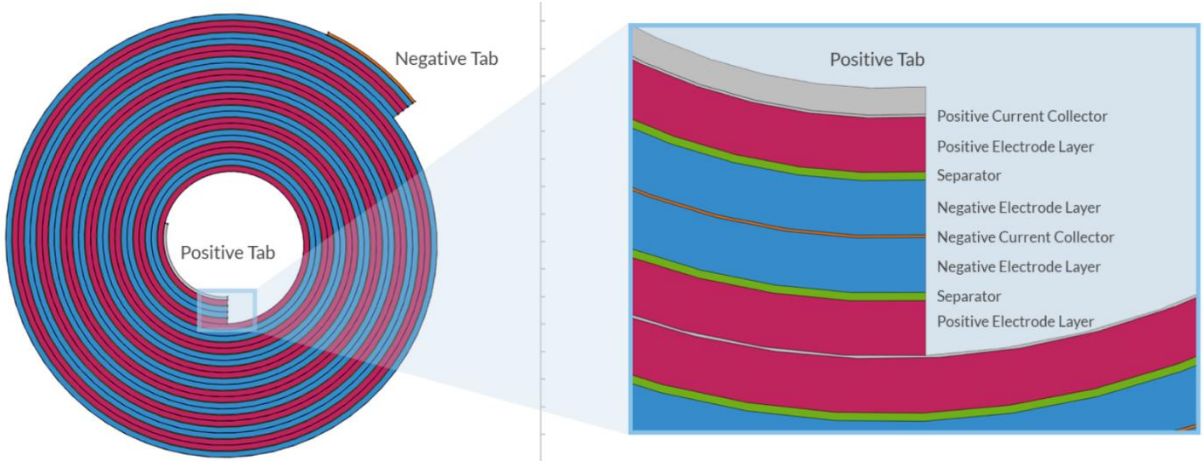

Figure 3-1: Cross-section of a spirally wound jelly roll [73]**.**

3.2.2 Mathematical approach

Figure 3-2 presents the simplified version of the battery cell in which the dimensions are defined. The thickness of one layer in the battery cell, δ_{total}, is then defined as the sum of positive current collector thickness, δ_c^P, positive electrode thickness, δ_e^P, separator thickness, δ_S, negative electrode thickness, δ_e^N, and negative current collector thickness, δ_c^N:

$$\delta_{total} = \delta_c^P + \delta_e^P + \delta_S + \delta_e^N + \delta_c^N \quad (3\text{-}1)$$

This allows to calculate the number of layers, N, as an integer within the defined dimension by the outer radius, r_n, of the battery cell:

$$N = \frac{r_n}{\delta_{total}} \quad (3\text{-}2)$$

Because the number of layers is rounded down to an integer number, there will be a space at the core of the battery cell. The radius of this empty cylinder is defined by the first radius, r_1:

$$r_1 = r_n - N \cdot \delta_{total} \quad (3\text{-}3)$$

The i[th] material layer radius, r_i, is calculated by summing the previous radius with the component thickness according to the repeating sequence of positive current collector – positive electrode – separator – negative electrode – negative current collector – negative electrode – separator – positive electrode – positive current collector – positive electrode - …:

$$r_i = r_{i-1} + \delta_{i^{th}\ component} \quad (3\text{-}4)$$

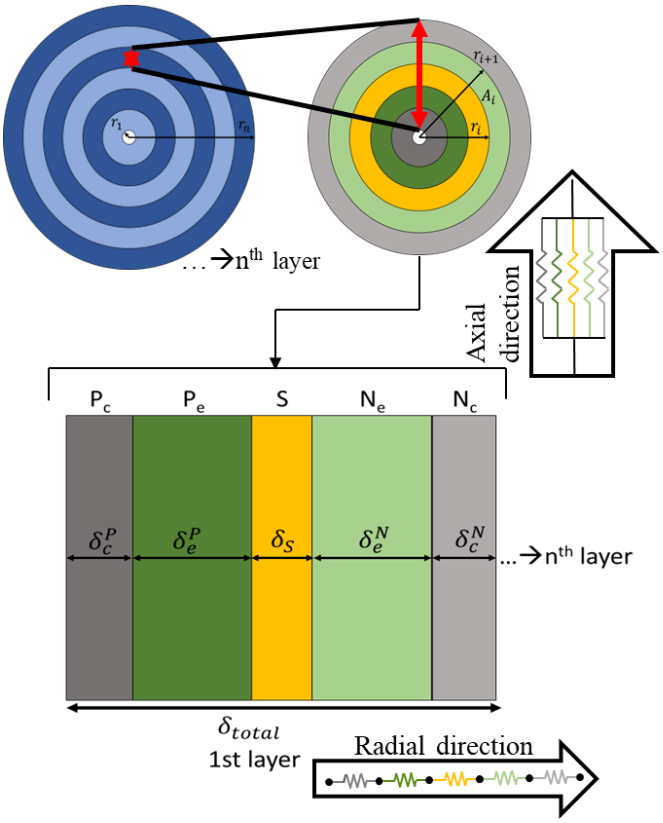

Figure 3-2: From battery cell to one cell layer; axial and parallel definition.

In Figure 3-2, axial and radial direction are defined. Depending on the direction considered, the equivalent material properties differ. The heat, q, in the radial direction, is calculated as a circuit of thermal resistors in series, whereas in the axial direction, this is calculated as a circuit of parallel thermal resistors. The resistance is a combination of the thickness, δ, area, A, and thermal conductivity, k. These equations are based on Fourier's equivalent thermal circuit for a composite wall [74].

$$q_{series} = \frac{T_1 - T_i}{\sum_{i=1}^{n-1} \frac{\delta_i}{k_i \cdot A_i}} \quad (3\text{-}5)$$

$$q_{parallel} = \frac{T_1 - T_i}{\sum_{i=1}^{n-1} \left(\frac{1}{\frac{\delta_i}{k_i \cdot A_i}}\right)} \quad (3\text{-}6)$$

Only the thermal conductivity is calculated for both directions k_{rad} and k_{ax} respectively by (3-7) and(3-8). Since the length in the parallel direction is the same for all components, it is not considered, thus only the orthogonal area counts for the axial direction:

$$k_{rad} = \frac{\ln\left(\frac{r_n}{r_1}\right)}{\sum_{i=1}^{n-1} \frac{\ln\left(\frac{r_{i+1}}{r_i}\right)}{k_i}} \quad (3\text{-}7)$$

$$k_{ax} = \frac{\sum_{i=1}^{n-1} k_i \cdot A_i}{A_{tot}} \quad (3\text{-}8)$$

Similarly to (3-8), the density and the specific heat capacity are calculated:

$$\rho_{eq} = \frac{\sum_{i=1}^{n-1} \rho_i \cdot A_i}{A_{tot}} \quad (3\text{-}9)$$

$$c_{p,eq} = \frac{\sum_{i=1}^{n-1} c_{p,i} \cdot A_i}{A_{tot}} \quad (3\text{-}10)$$

The thermal capacity, C_{th}, can be calculated as the product of specific heat, density and the volume of the battery cell defined by its dimensions, the radius, and the length L:

$$C_{th} = c_{eq} \cdot \rho_{eq} \cdot \pi \cdot {r_n}^2 \cdot L \quad (3\text{-}11)$$

Equation (3-8) is then further modified to calculate the equivalent electrical conductivity:

$$\sigma_{+,eq} = \frac{\sum_{i=1}^{n-1} \sigma_{i,P_c} * A_{i,P_c} + \sum_{i=1}^{n-1} \sigma_{i,P_e} * A_{i,P_e}}{A_{total(P_c,P_e)}} \quad (3\text{-}12)$$

$$\sigma_{-,eq} = \frac{\sum_{i=1}^{n-1} \sigma_{i,N_c} * A_{i,N_c} + \sum_{i=1}^{n-1} \sigma_{i,N_e} * A_{i,N_e}}{A_{total(N_c,N_e)}} \quad (3\text{-}13)$$

3.2.3 Numerical validation

The validation of the model consists of two parts. This section describes the first part in which the numerical approach is compared to a model found in the literature [11].

During the validation process, an 18650 – $LiFePO_4$.cell was used to validate the proposed approach in 3.2.2. Table 3-2 presents the specifications of this cell.

Table 3-2: LiFePO4-18650- 1,3 Ah nominal specifications [11]**.**

Item	Specification
Nominal Capacity	1,3 Ah
Nominal Voltage	3,2 V
Cell Diameter	18,2 ± 0,3 mm
Cell Height	64,8 ± 0,3 mm
End-of-charge Voltage	3,65 V
End-of-discharge Voltage	2,5 V

Table 3-3 gives the properties of the characterizing components [11]. Throughout the work, it is assumed that the same materials are used for the components. The physical properties of these elements are the same for all lithium-ion cylindrical cells. Only the thickness for each component can vary, which will affect the equivalent material properties of the entire cell. The components' thickness given in the table is considered the base model for further development.

Table 3-3: LFP cell components' material properties [11]**.**

Component	thickness, δ [µm]	thermal conductivity, k [W/m·K]	electrical conductivity, σ [S/m]	density, ρ [kg/m^3]	specific heat capacity, c_p [J/kg·K]
positive current collector, P_c	10	170	$3{,}5 \cdot 10^7$	2770	875
positive electrode, P_e	130	0,2	0,04	3600	750
separator, S	10	0,3344	-	1009	1978
negative electrode, N_e	90	1,04	100	1347	1437
negative current collector, N_c	20	398	$5{,}98 \cdot 10^7$	8933	385

For this configuration, the equivalent thermal conductivity is calculated and compared to the approach from the article. The results are presented in Table 3-4.

Table 3-4: Equivalent material properties of the base model.

	radial thermal conductivity, k_{rad} [W/m·K]	**axial thermal conductivity, k_{ax} [W/m·K]**
thesis' approach	0,324	37,63
article's equation [11]	0,339	37,63

From Table 3-4, there is no difference in the axial direction, but in the radial direction, the difference is 4,42%. By simulating both approaches in CFD, the effect of this difference is further checked in paragraph 3.3.4. Since the radial thermal conductivity is much smaller than in the axial direction, only a small temperature change is expected.

3.3 CFD model

3.3.1 Multi scale multi domain - MSMD

The goal is to determine the temperature distribution within the cell through thermal analysis. It is challenging to model a lithium-ion battery because of its multi-domain, multi-physics nature. In the anode-separator-cathode sandwich layers, the Li-ion transport takes place. In the active material, this occurs at the atomic length scale. The multi-scale-multi-domain or MSMD deals with different physics in different solution domains. Furthermore, it is important to mention that this equation only relates to the cell itself as a black box. This means that the convection of heat to the environment is not considered [75].

Battery thermal and electrical fields are solved for temperature T in the CFD domain at the battery cell's scale using the following differential equation:

$$\frac{\partial(\rho \cdot c_p \cdot T)}{\partial t} - \nabla \cdot (k \cdot \nabla \cdot T) = \sigma_+ \cdot |\nabla \cdot \varphi_+|^2 + \sigma_- \cdot |\nabla \cdot \varphi_-|^2 + \dot{q}_{ECh} + \dot{q}_{short} + \dot{q}_{abuse} \quad (3\text{-}14)$$

j_{ECh} and $\dot{q}_{ECh}$ are the current transfer rate and the electrochemical reaction heat due to electrochemical reactions. $\dot{q}_{abuse}$ is the heat generation due to the thermal runaway reactions under thermal abuse conditions and equals zero in normal operation, which is the case. φ_+ and φ_- represent the phase potentials for the positive and negative electrodes respectively and are derived from the equations (3-15) and (3-16) underneath. j_{short} and $\dot{q}_{short}$ represent the current transfer rate and heat generation due to the battery's internal short-circuit. In this case, it is zero because there is no internal short-circuit.

$$\nabla \cdot (\sigma_+ \cdot \nabla \cdot \varphi_+) = -(j_{ECh} - j_{short}) \quad (3\text{-}15)$$

$$\nabla \cdot (\sigma_- \cdot \nabla \cdot \varphi_-) = j_{ECh} - j_{short} \quad (3\text{-}16)$$

3.3.2 Equivalent circuit model - ECM

To compute the parameters depending on the electrochemical reactions an electrochemical submodel is used. There exists a wide range of such submodels. The submodel chosen for this experiment is the Equivalent Circuit Model or ECM:

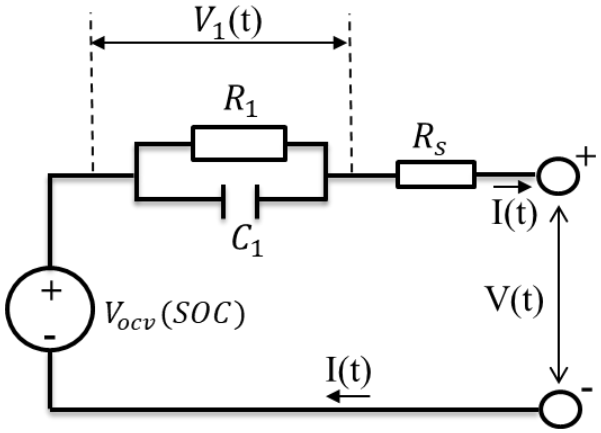

Figure 3-3: Electric circuit used in the ECM model.

By solving the electric circuit relations, the voltage-current relation can be obtained:

$$V = V_{ocv}(soc) - V_1 - R_s(soc) \cdot I(t) \quad (3\text{-}17)$$

$$\frac{dV_1}{dt} = -\frac{1}{R_1(soc)C_1(soc)} \cdot V_1 - \frac{1}{C_1(soc)} \cdot I(t) \quad (3\text{-}18)$$

$$\frac{d(soc)}{dt} = \frac{I(t)}{3600 \cdot Q_{ref}} \quad (3\text{-}19)$$

Where V stands for the battery cell voltage and can either be calculated directly from the circuit solution or by the difference in phase potential from the MSMD solution method. For a given battery the open-circuit voltage V_{ocv}, the ohmic resistance R_s, charge rate resistance R_1 and capacitance C_1 of the ECM depending on the battery state of charge and temperature. In Ansys fluent, this relationship is given by a two-dimensional structured table to define each parameter as a function of SOC and temperature. The 2D table method allows to account for the temperature effect [76]–[78].

The values for the ECM are obtained from experimental studies on the 32700 LFP cell according to the methodology described by A. Broatch et al. [79]. The curves and the data for the electrical parameter are given under 2C condition at four levels of temperature (0 °C, 10 °C, 20 °C, and 40 °C). The ohmic resistance, charge rate resistance, charge rate capacitance and open-circuit voltage are given in Figure 3-4, Figure 3-5, Figure 3-6, and Figure 3-7 respectively. Generally, when temperature increases, the resistance and capacitance decrease.

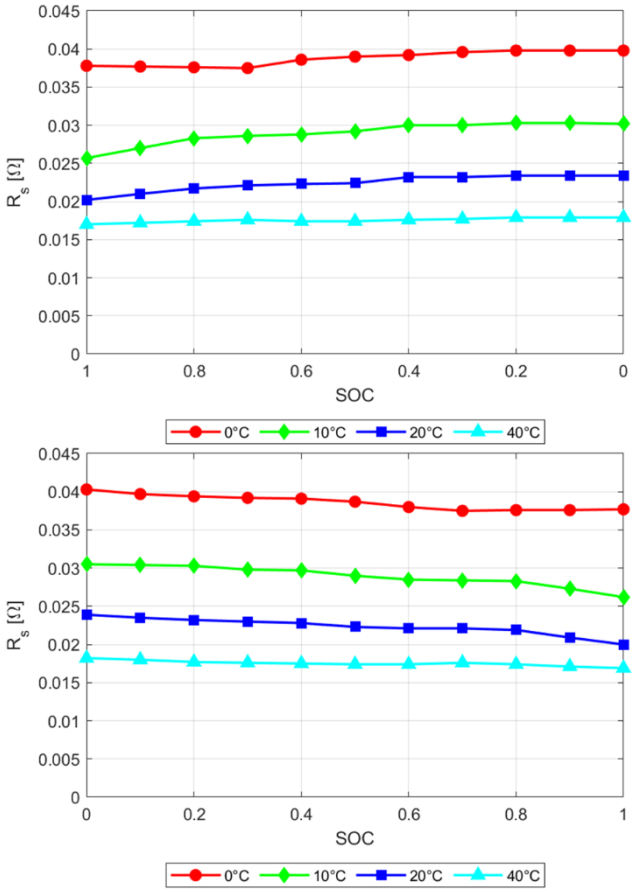

Figure 3-4: Ohmic resistance R_s for discharging (top) and charging (bottom) conditions.

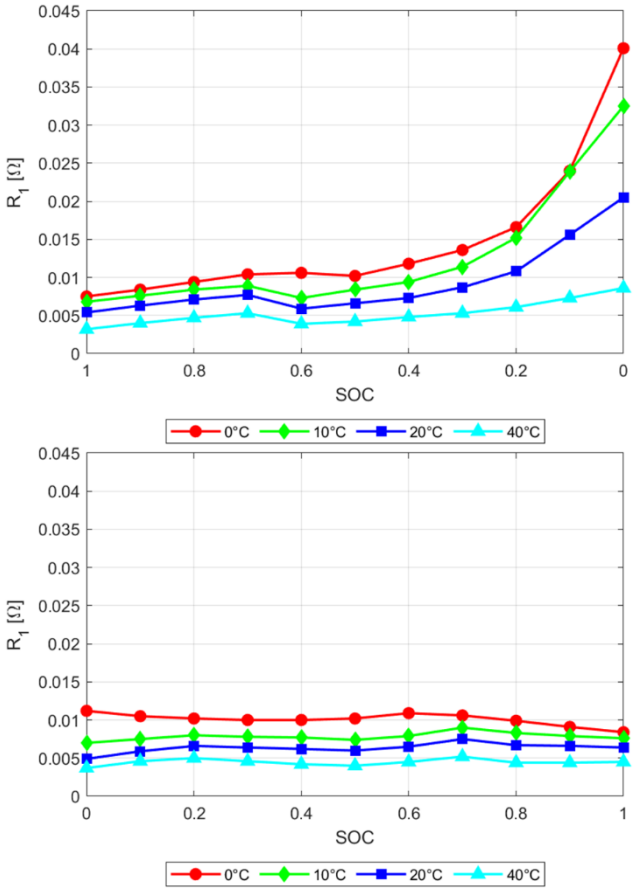

Figure 3-5: Charge rate resistance R_1 for discharging (top) and charging (bottom) conditions.

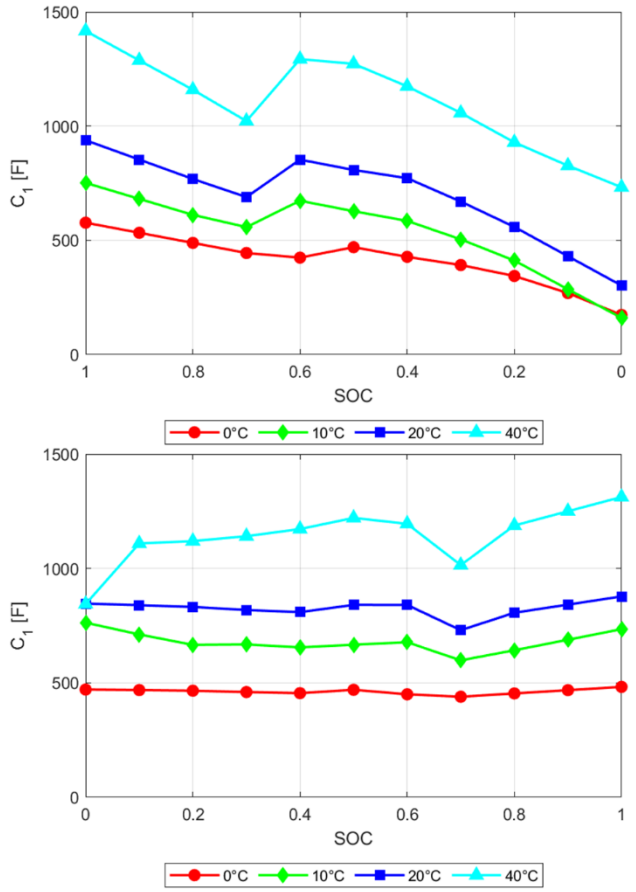

Figure 3-6: Charge rate capacitance for discharging (top) and charging (bottom) conditions.

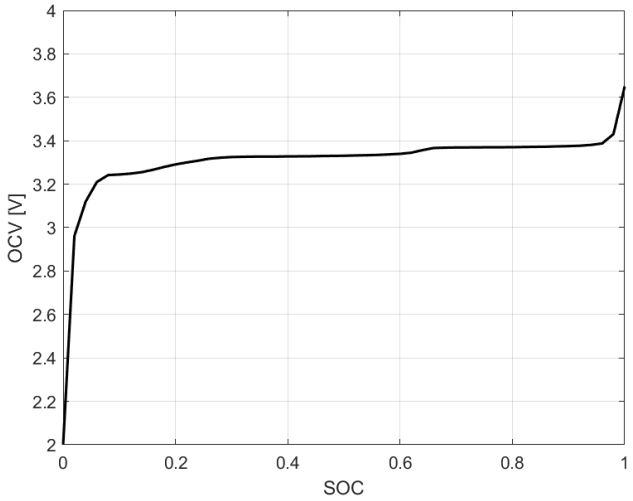

Figure 3-7: Open-circuit voltage OCV.

From the ECM the electrochemical current transfer rate and heat generation are calculated as follows:

$$j_{ECh} = I \cdot \frac{Q_{nom}}{Q_{ref} \cdot Vol} \quad (3\text{-}20)$$

$$\dot{q}_{ECh} = j_{ECh} \cdot [V_{ocv} - V - T \cdot \frac{dU}{dT}] \quad (3\text{-}21)$$

Here, I is the current and Vol the volume of the battery. In this case, the reference capacity Q_{ref} is the same as the nominal capacity Q_{nom}.

3.3.3 Mesh independence study

When doing CFD simulations it is important to check whether the solution is mesh dependent. A coarse mesh could give wrong results, but a very fine mesh can cause large calculation times. To find the adequate mesh, several base mesh sizes were run while monitoring the maximum temperature rise at the core of the cell. The boundary conditions are kept the same for each simulation, thus the same physical properties, discharging at 2C rate and ambient temperature at 20°C. When the mesh had a base size of 1,5 mm or smaller, the monitored temperature results did not change anymore. The mesh independence study is represented in Figure 3-8. For further simulations, the optimal mesh size of 1,5 mm is used.

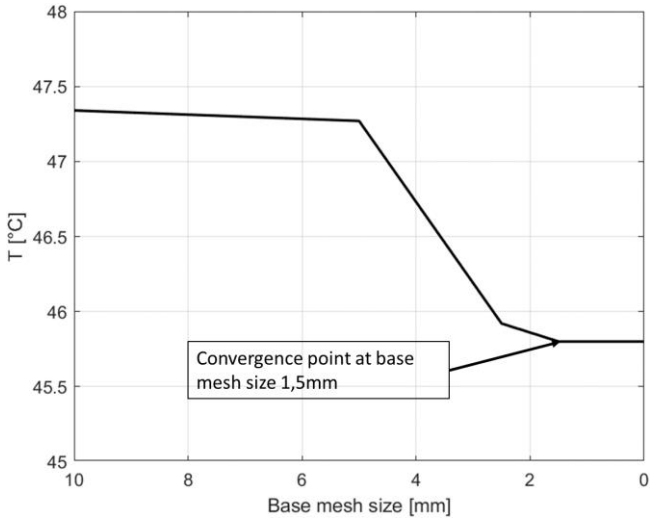

Figure 3-8: Mesh independence study.

3.3.4 Validation of the CFD model

Figure 3-9 shows the comparison of CFD simulation results with experimental results. The experimental data and the 'CFD results 1' are obtained by Saw et al. [11]. 'CFD results 2' represents the simulation results of the approach proposed in 3.2 of this master's thesis.

The 18650 LFP cell with a charge capacity of 1,3 Ah described in Table 3-2 and Table 3-3 is used. For the self-conducted CFD results, the obtained ECM parameters of the 32700 cell in 3.3.2 are assumed to be the same for the 18650 cell. The boundary conditions are kept the same as described in 3.3.3, except, the c-rate was changed to 3C charging condition.

In Figure 3-9, on the left, the temperature evolution for the experimental and both of the CFD results are plotted. The graph portrays that the 'CFD results 1' and 'CFD results 2' fit closely to the experimental data. On the right, the temperature difference between both of the CFD results with the experimental data is shown. The difference between 'CFD results 2' and the experimental data is only 1,4°C at the most. The results obtained by the novel approach in this master's thesis fit even slightly better with the experimental data. Both figures conclude that the new approach for calculating the thermal properties of the cell is validated for obtaining trustable results.

The impact of the small difference in radial conductivity between the article's approach and the novel approach is negligible in this case. However, given the slightly better fit, the new approach is more physical and can be seen as a good way of calculating the equivalent radial conductivity for battery cells. For bigger cell dimensions there is a possibility that the differences in radial conductivity would be higher, thus it is more important to calculate the radial conductivity.

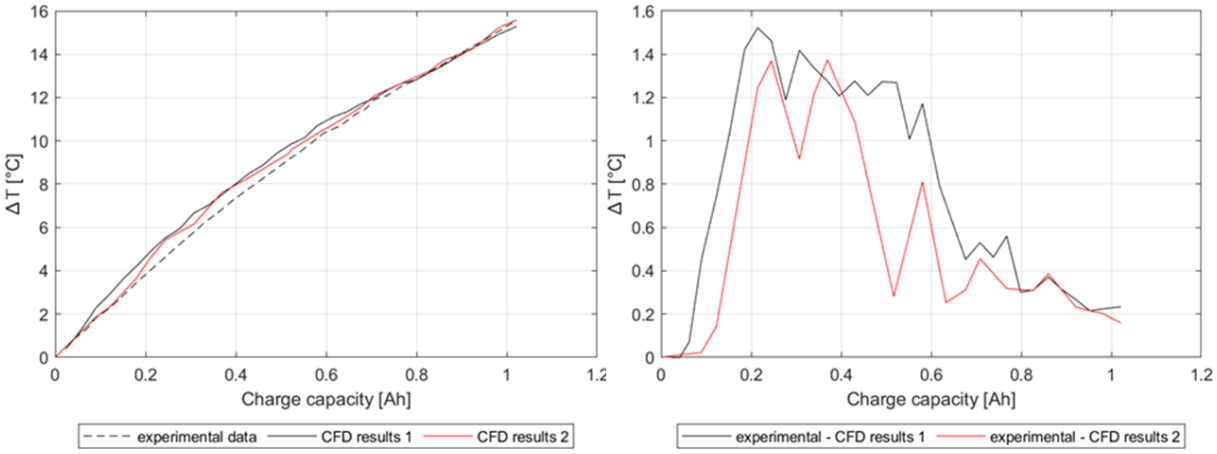

Figure 3-9: Validation of the CFD model: absolute temperature difference (left); relative temperature difference to the experimental temperature (right) [11]**.**

3.4 Effect of battery shell

Figure 3-10: Broken canister/shell of a battery cell.

So far, only the internal components' properties were included in the calculations for the equivalent material properties. However, the outer layer of a cell, also known as the shell or canister (see Figure 3-10) may also impact these properties. The aim of the shell is not only to provide mechanical integrity to the lithium-ion battery upon external mechanical loading but also to prevent dust and liquids from entering the battery cell [80]. The properties of the shell are given in Table 3-5.

Table 3-5: Canister/shell properties.

Thickness, δ [µm] [81]	**Thermal conductivity, k [W/m·K]** [82]
200	0,638

To check whether to include the shell thickness in the calculations, the thermal conductivity is calculated for both cases, with and without the canister:

Table 3-6: Equivalent thermal conductivity with and without battery cell shell

	radial thermal conductivity, k_{rad} [W/m·K]	**axial thermal conductivity, k_{ax} [W/m·K]**
with shell	0,32446	37,06
without shell	0,32404	37,63

The difference in Table 3-6 for the thermal conductivity is very low. More specifically, the difference between with shell and without shell is only 1,5% for the axial thermal conductivity and even less, 0,13%, for the radial thermal conductivity. These slight differences conclude that the shell has a negligible impact on the overall equivalent material properties. Henceforth, the shell is not included in the CFD study. One main reason for this is the fact that the canister is a non-repeating material layer, it only sits on the outer surface.

3.5 DOE-study

To better understand the relationship between the thickness of cell components, thermal conductivity and thermal capacity, a design of experiment (DOE) study is set up. The effect of each component thickness on the parameters is represented by a Pareto chart and a main effects plot (Figure 3-11, Figure 3-12 and Figure 3-13). These figures portrayed that when a bar crosses the vertical line, represented with blue colour, in the Pareto chart, it means that the represented factor influences the outcome significantly. The calculations are done in the software 'Statgraphics 18'. The base model, described in Table 3-3, is taken as the centre point for the calculations. The minimum and maximum thicknesses considered are defined in Table 3-7.

Table 3-7: DOE – definition of minimum, centre point and maximum values for the thickness.

	δ_e^P [µm]	δ_e^P [µm]	δ_s [µm]	δ_e^P [µm]	δ_e^P [µm]
minimum = 50%	5	65	5	45	10
centre point = 100%	10	130	10	90	20
maximum = 150%	15	195	15	135	40

The DOE generated 33 experiments. 32 of them are all unique combinations of maximum or minimum thickness for each component. The 33rd combination of component thicknesses is the centre point.

3.5.1 Effect of components' thickness on the radial thermal conductivity

Figure 3-11 gives the relationship between the components' thickness and the radial conductivity. The thickness of the positive electrode affects the radial conductivity the most. The correlation is inversely proportional. When this thickness is reduced, the conductivity in the radial direction increases. The effect of the negative electrode thickness is half as strong as the positive electrode thickness effect. In addition, the correlation between the negative electrode and radial conductivity is proportional to each other. In detail, when the negative electrode thickness is increased, the radial conductivity also increases. The radial conductivity is proportional to the thickness of both current collectors, positive and negative. The effect of the separator is very small compared to all other components.

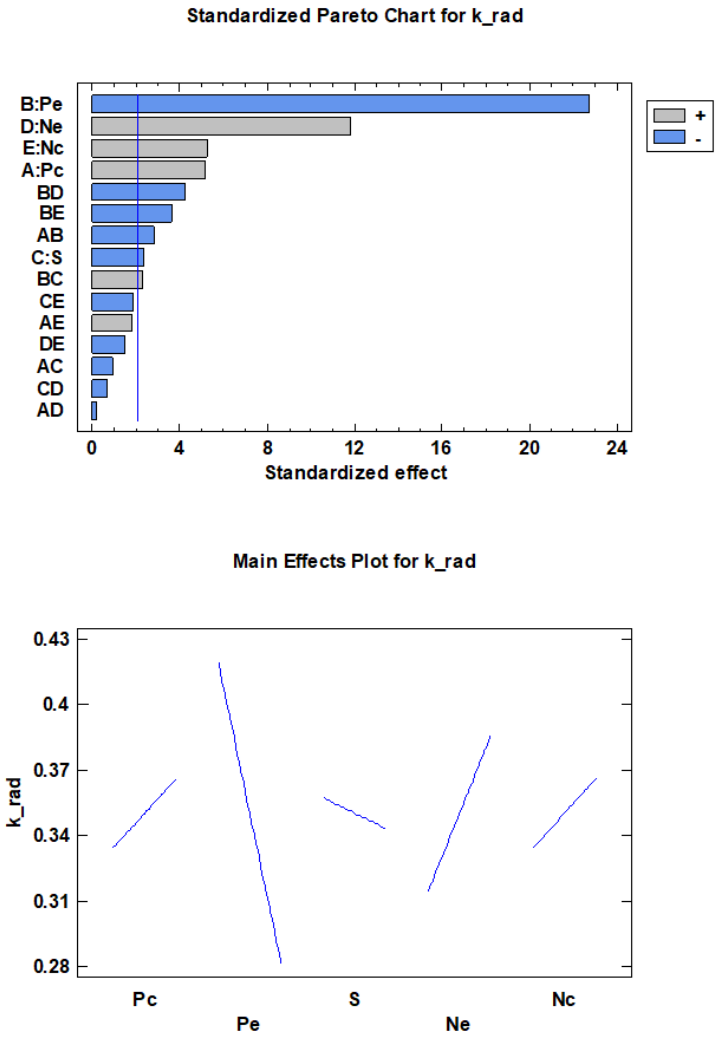

Figure 3-11: Pareto chart (upper) and main effects plot (lower) for the radial conductivity.

3.5.2 Effect of components' thickness on the axial thermal conductivity

Figure 3-12 confirms that the thickness of the negative current collector affects the axial thermal conductivity the most, in such a way that the axial conductivity increases with an increase in its thickness. Thus, the correlation between the negative current collector and the axial thermal conductivity is inversely proportional. A proportional correlation can be found between the electrodes, both negative and positive, and the thermal axial conductivity. So, whenever the thickness of one or both electrodes is reduced, the axial thermal conductivity will rise. The positive current collector affects the axial thermal conductivity way less than the radial thermal conductivity. The effect of the separator is the same as for the radial conductivity.

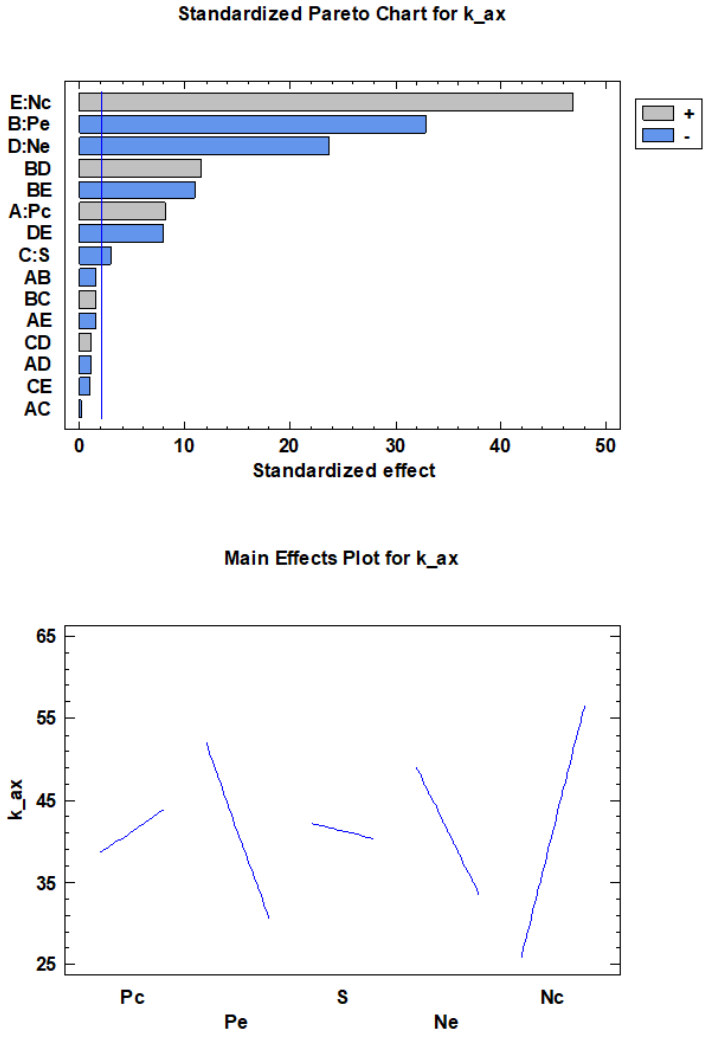

Figure 3-12: Pareto chart (upper) and main effects plot (lower) for the axial conductivity.

3.5.3 Effect of components' thickness on the thermal capacity

Formula (3-11) states that thermal capacity is influenced by density, specific heat, and volume. The dimensions of the cell are fixed, and so is the volume, the thermal capacity only depends on the density and the specific heat. Since these two are material-related properties, the equivalent density and specific heat are affected by the thickness of the cell components. This relationship is given by equations (3-9) and (3-10) in section 3.2.2. How the thermal capacity behaves depending on the thickness of the cell components is represented in Figure 3-13. It demonstrated that the negative current collector affects the thermal capacity proportionally as well as influences the thermal capacity the most. The correlation between the electrodes, both positive and negative, and the thermal capacity is inversely proportional. Neither the separator nor the positive current collector affects the thermal capacity remarkably. Their effect is even negligible.

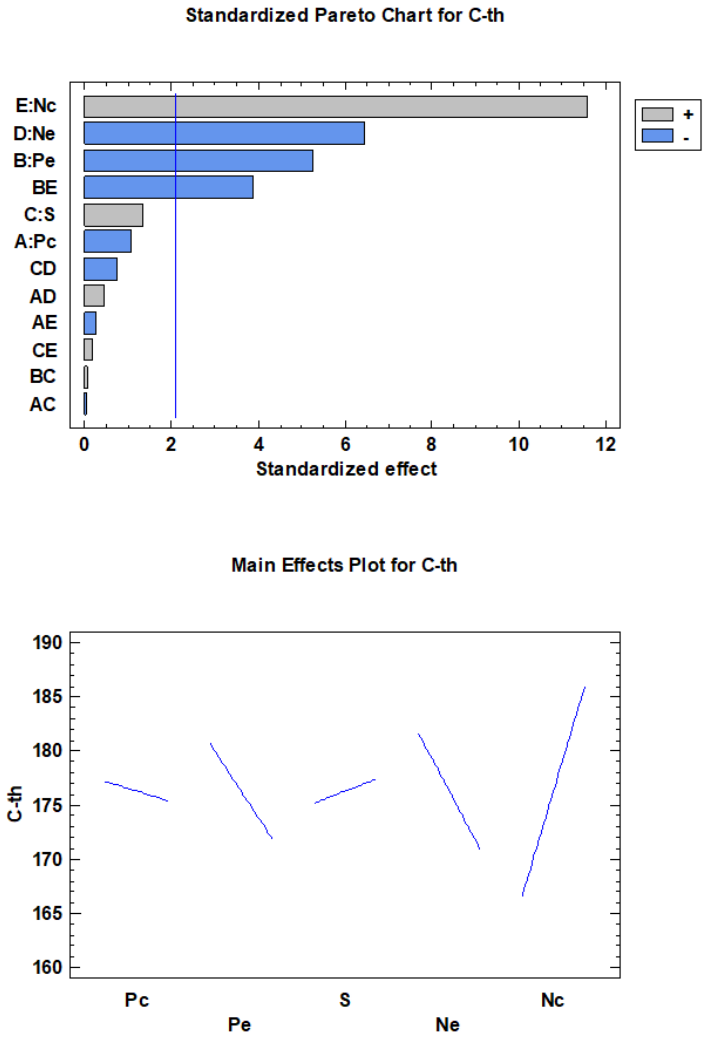

Figure 3-13: Pareto chart (upper) and main effects plot (lower) for the thermal capacity.

3.5.4 Summary of the DOE.

Table 3-8 summarizes the previous sections by giving a 'score' for each relation between component and parameter. The minus sign '-' represents an inversely proportional correlation, whereas the plus sign '+' represents a proportional correlation. According to the impact of the component, the number of signs differs.

Table 3-8: Component's thickness effect on thermal conductivity and capacity.

component	radial thermal conductivity, k_{rad}	axial thermal conductivity, k_{ax}	thermal capacity, C_{th}
P_c	+	+	/
P_e	- - - -	- - -	- -
S	/	/	/
N_e	++	- -	- -
N_c	+	++++	++++

4 CFD-STUDY RESULTS

4.1 Assumptions

As mentioned earlier the DOE result generated overall 33 possible configurations. Since it is proved in 3.3.4 that the impact of the radial conductivity on the temperature curve is very small, the axial thermal conductivity is seen as the major thermal input variable. Nevertheless, some configurations resulted in the same axial thermal conductivity. Furthermore, the density and specific heat, which are calculated in the same way as the axial thermal conductivity, also yield the same values. In turn, the heat capacity will also be the same whenever the axial thermal conductivity yielded the same. In these situations, only one combination was considered. As a result, the overall computing time is reduced due to the reduction of the total number of cases to 18 instead of 33, including the base model.

As mentioned in 3.3.4, it is considered that the ECM for all cases is the same so that every cylindrical lithium-ion cell shares the same electrical properties except for the electrical conductivity. This means that for every case of the DOE, the resistances and capacitance are the same as described in section 3.3.2.

The electrical specifications were given in Table 3-1 in section 3.1. On top of that, just like in paragraph 3.2.3, the same material properties given in Table 3-3 are assumed. Only the internal configuration of the cell differs, more specifically, the components' thickness. This leads to different internal features, such as the number of layers and the first radius. Finally, the equivalent material properties aren't the same, thus the cell has different thermal characteristics.

For every case, two simulations are executed, charging, and discharging. Because the experimental temperature curves and the ECM parameters are both known under 2C condition and an ambient temperature of 20°C, both situations were conducted for these boundary conditions.

The experimental data were obtained internally within CMT, following the method described by Broatch et al. [79]. The experiment is conducted three times, and the average temperature of the three experiments was taken as the represented experimental temperature in Figure 4-1 and Figure 4-2. Since this is measured by a thermocouple, which sits halfway on the outer surface of the cell, a banded surface region is defined in the CFD model at which the temperature is monitored.

4.2 Results for charging

The simulation results, more specifically the cell surface temperatures for charging, are portrayed in Figure 4-1. The initial state of charge is 0,038. In the left graph, a dip can be observed in the experimental data. This dip is also retrieved in the ambient temperature curve and was caused by frigid air blown inside the climate chamber to maintain the ambient temperature after a certain threshold is exceeded and consequently triggered the ventilation system. Furthermore, this dip causes a deviation on the measured temperature curve starting from a state of charge 0,5 and on. This main effect induces a peak in the relative temperature difference plot on the right side and an upwards shift of the difference. However, before the dip, case 11 suits the experimental data the best, where the difference fluctuates only between 0 °C and 0,27 °C. After the dip, the temperature differs between 0,96 °C and 1,89 °C, which is still considered to be good. The end temperature of case 11 is 31,47°C, whereas the end temperature of the experiment is 29,82°C so in the end the maximum difference is 5,5 %. The worst case for charging is case 5 for which the end-of-charge temperature is 33,39°C, which results in a deviation of 12 %.

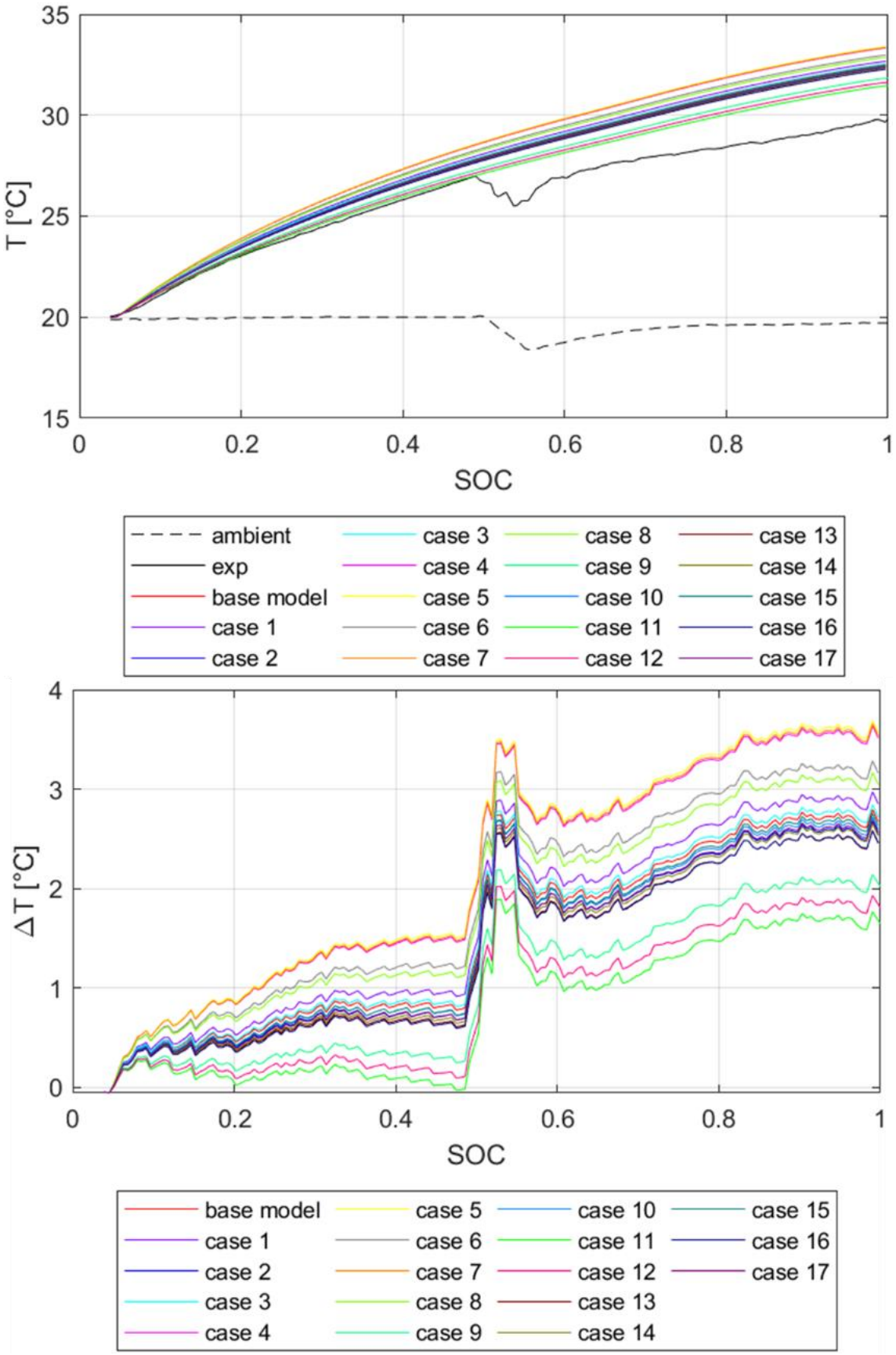

Figure 4-1: Absolute temperature plot (top); Relative temperature difference with experimental data (bottom) for charging.

4.3 Results for discharging

The discharging results are presented in Figure 4-2. Contrary to the ambient charging temperature, the ambient temperature for discharging remains constant. In the figure at the top, the experimental temperature curve makes an S-shape. However, the CFD results don't follow this trend. The results deviate from the experimental at a temperature of 30°C. One main reason for this is the fact that the ECM parameters during simulation are only described for 0°C, 10°C, 20°C and 40°C. From the literature, it is known that the temperature of the battery itself affects the ECM parameters [77], [78]. However, the parameters of the ECM are not known at a temperature of 30°C, furthermore, the ECM does not interpolate between 20°C and 40°C in the CFD domain for this thesis. Henceforth, the ECM parameters obtained at 20°C have been followed up to 39,99°C of the cell, thus, the simulation results are not able to follow the experimental curve.

For the chosen case 11 in 4.2, the reported end temperature is 43,11 °C, whereas experimentally, the end of discharge temperature is 45 °C. This is a 4,2 % difference. For case 5, the temperature after discharging is 46,79 °C, which differs by 4 % from the experimental. However, the temperature difference between the simulated temperature curve and the measured temperature fluctuates between -2,44 °C and 1,42 °C for case 11. For case 5, this ranges from 1,46 °C to 4,56 °C.

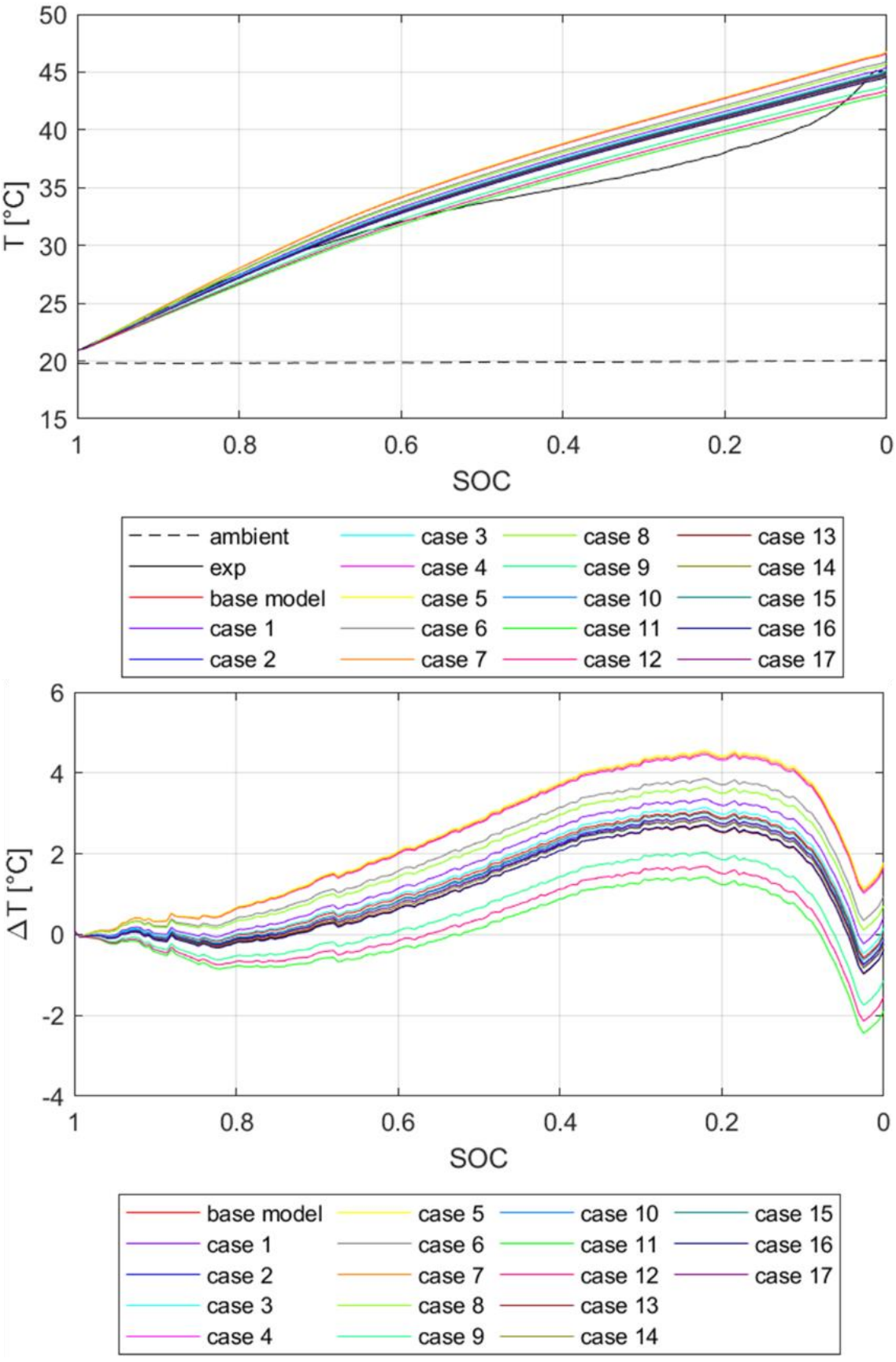

Figure 4-2: Absolute temperature plot (top); Relative temperature difference with experimental data (bottom) for discharging.

4.4 Case 11

From 4.3, and especially from 4.2, case 11 fits, in general, the best to the experimental data. The configuration and equivalent material properties are described in Table 4-1 underneath.

Table 4-1: Case 11

$\delta_{total} = \delta_c^P + \delta_e^P + \delta_S + \delta_e^N + \delta_c^N$ [µm]		160 = 5 + 65 + 15 + 45 + 30
thermal conductivity, k_{eq} [W/m·K]	radial	0,377
	axial	80,91
density, ρ [kg/m^3]		3.704
specific heat capacity, c_p [J/kg·K]		994
electrical conductivity, σ [S/m]	positive	1.083.291
	negative	11.305.031
thermal capacity, C_{th} [J/K]		207,28

Above all, case 11 presented for both cases, charging, and discharging, the temperature curve closest to the experimental curve. This means it is, thermally speaking, the most optimal configuration from all the presented cases.

Additionally, the temperature evolution is studied at the core and on the surface of the cell from case 11. The temperature monitored by the defined thermocouple and at the core is plotted along the state of charge in Figure 4-3 for charging and in Figure 4-4 for discharging. The difference between the temperature at the core and on the surface grows near the end of (dis)charge. For charging this difference is only 0,62°C, whereas for discharging this is 1,23°C, which is still very small. Consequently, the surface temperature can be accepted as the overall cell temperature.

As mentioned in 4.1 the thermocouple is positioned on the surface of the cell. Figure 4-5 and Figure 4-6 present the evolution of temperature distribution during charging and discharging, respectively, on the surface (top) and at the core plane (bottom) of the cell for several states of charge (0,00; 0,33; 0,67 and 1,00). In general, the cell temperature is uniform on the surface. In the radial direction, the temperature is the hottest at the core and gets colder near the cell surface. However, as mentioned above, this difference is very small. The temperature scale is the same for the contour plots of the cell surface, while the temperature scale of the core planes varies for each soc to portray the subtle radial temperature gradient.

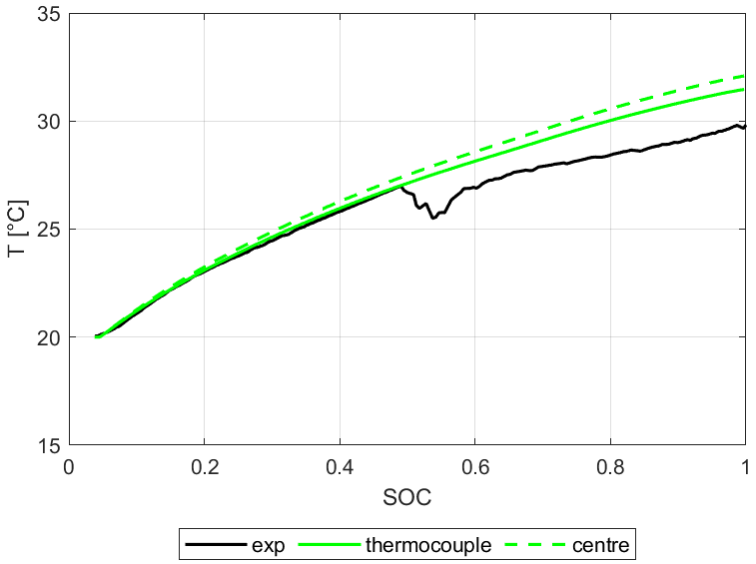

Figure 4-3: Charging temperature curve at the cell centre and from the thermocouple on the surface.

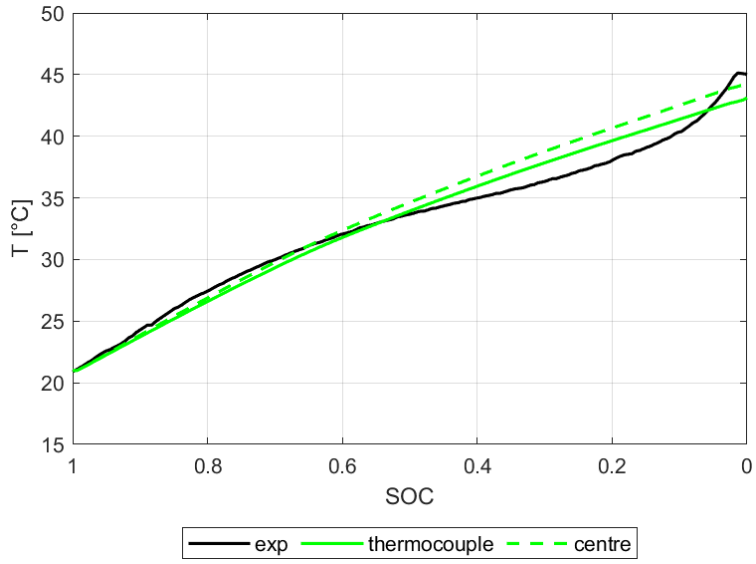

Figure 4-4: Discharging temperature curve at the cell centre and from the thermocouple on the surface.

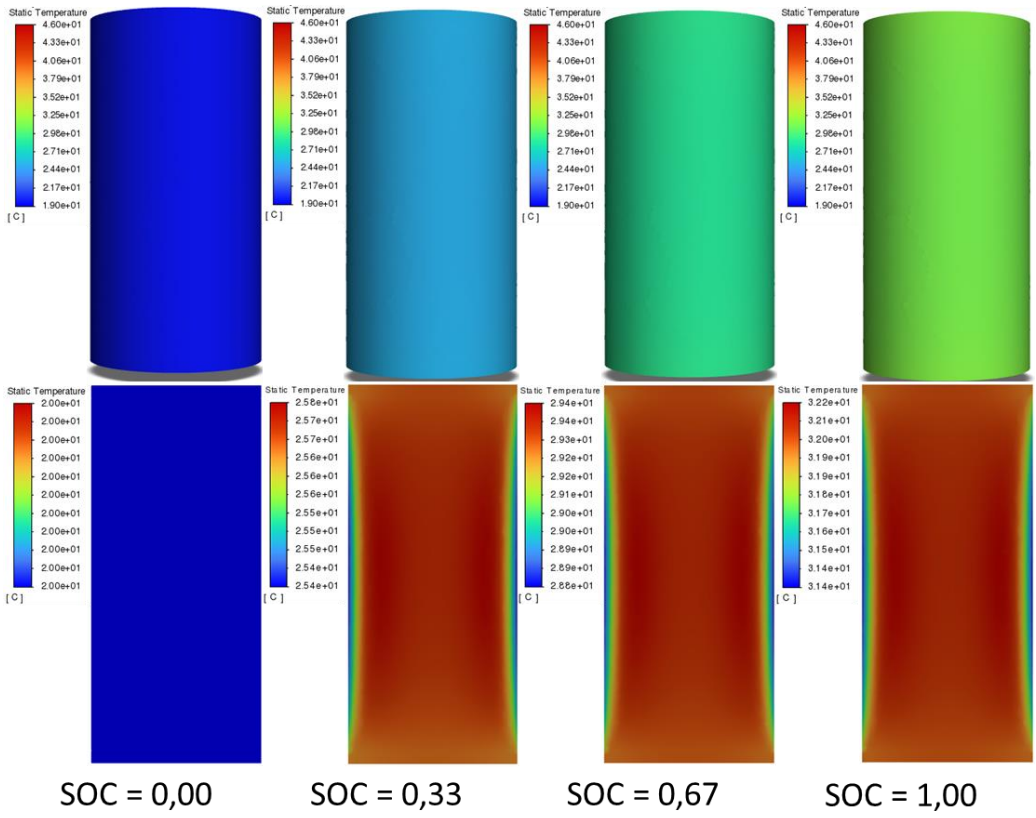

Figure 4-5: Temperature evolution on the cell surface (top) and in the inner core plane (bottom) during charging for case 11.

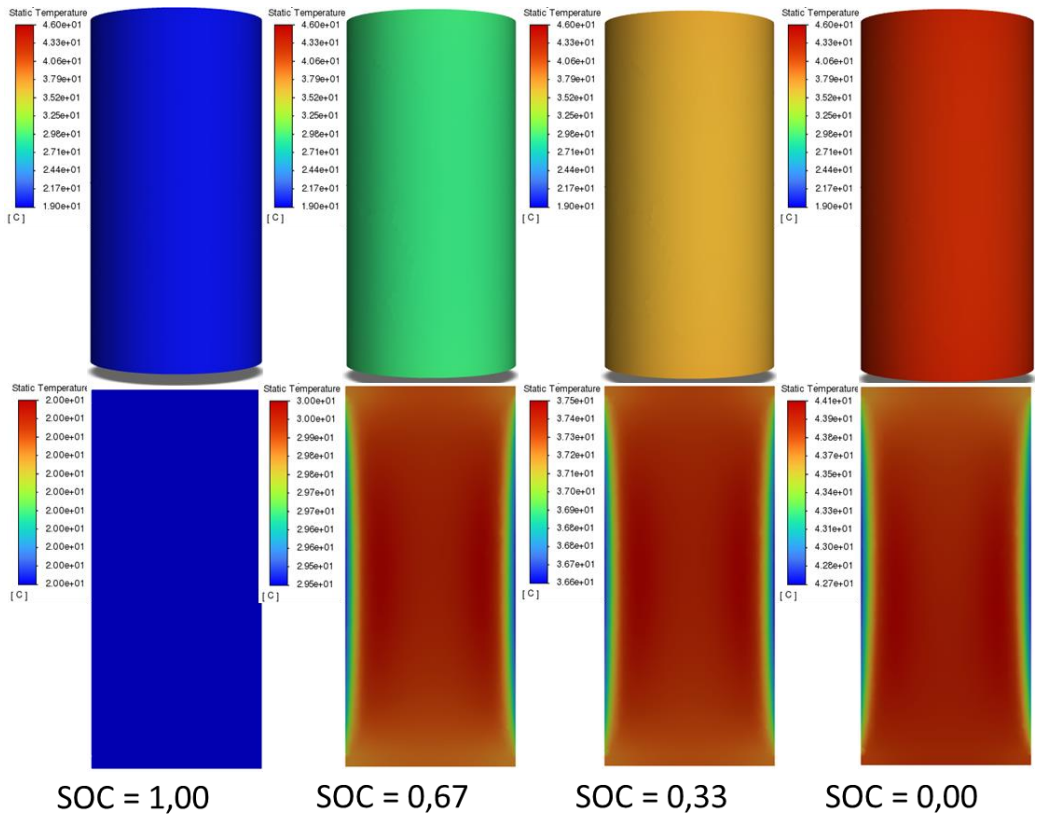

Figure 4-6: temperature evolution on the cell surface (top) and in the inner core plane (bottom) during discharging for case 11.

5 GENERAL CONCLUSIONS AND FURTHER RECOMMENDATIONS

The goal of this work was to analyse the effects of varying the characterising material thicknesses on the cylindrical cell's thermal response. This was conducted through a CFD study of several possible scenarios generated by a design of experiments. Since the CFD software only allows the definition of the properties of the entire battery cell as a single element, a new numerical model has been developed to precisely determine the equivalent thermal properties. Furthermore, the right model for the CFD approach was chosen and explained. After conducting the simulations, the accomplished data was compared with internally retrieved experimental data to give a detailed thermal study. The approach was compared and validated with data from external sources.

In conclusion, the methodology stated in this work is useful to determine the inner configuration of a cylindrical cell and shows its important impact on the equivalent material properties, which in turn characterise the thermal behaviour of the cell.

For future work, its recommended to extend the use of the methodology for different charge rates and temperatures. Further investigation regarding electrical conductivity can be useful since it affects the temperature via the MSMD model. Since the generated combinations from the DOE are discontinuous, it would be interesting to investigate configurations in between these discontinuities. Lastly, it could be useful to incorporate convection between the cell and the surrounding air. These suggestions would generate valuable insights and make it possible to design a system to manage the thermal behaviour of the battery.

6 BUDGET

To calculate the estimated cost of this TFM, a budget analysis is conducted. The cost breakdown includes expenses related to HR, equipment, and software packages.

The following points are considered for the calculation of the budget:

- Indirect costs: These are costs that cannot be directly associated with the given unit of the work and are therefore considered as a percentage of the direct costs. Some examples of indirect costs are rent, salaries and maintenance. In this work, an indirect cost of 15% is considered.
- Overheads correspond to the costs of carrying out an activity (costs made by CMT, for example, logistics, personnel, …). They are usually between 9% and 16% depending on the work carried out. In this case, 13% overheads are considered.
- VAT is already included in the prices that appear in the tables. Only in the end VAT is subtracted from the total price to get an idea of the total budget without VAT. The general VAT in Spain is 21% [83].
- Ten per cent of the total budget is calculated as profit for when the institution wants to sell the research information.

6.1 Human resources

This part summarizes the retribution received by the participants in the project. Three people are engaged in the TFM: the student and author of the work, the professor as the first supervisor and the PhD student as the second supervisor.

The salary of the student is considered as if the student would be a young graduate in MSc of engineering technology. In this case, he would earn €/hour. As for the PhD student, a salary of 50 €/hour is chosen. The hourly income of the more experienced professor is 60 €/hour. The social security contributions are included in the wages.

The workload of one ECTS is considered to be between 25 and 30 hours [84]. The TFM is registered as 20 ECTS. This means the student must put between 500 and 600 hours of work into the project.

The cost for each one regarding the time they put into the project is shown in Table 6-1.

Table 6-1: Cost associated with human resources.

	Total time (h)	**Hourly retribution (€/h)**	**Subtotal (€)**
Student	500	46	23.000,00
supervisor 1: professor	24	60	1.440,00
supervisor 2: PhD student	75	50	3.750,00
		Total	**28.190,00**

6.2 Equipment costs

The cost associated with the equipment can be distinguished into three categories. These costs include self-contributed resources, facility resources and additional resources. For all the expenses, VAT is already included in the price.

The only self-contributed cost is the laptop. Other small costs such as pencils, a mouse, and paper are not taken into account. The cost of the device, a Lenovo Legion 15", is €1649. A lifespan of five years is considered.

The facility costs for testing materials, computers, etc. are stated below:

- Cell used for testing: €20.
- Thermocouple: €20/thermocouple.
- Battery tester: total cost €2000, used for 5 months (amortization) of which 500 hours are used for this TFM.
- Climatic chamber: total cost €4000, used for 5 months, 500 hours.
- Data acquisition system: €2290.88, 5 months, 500 hours.
- Thermographic camera: -
- Holder: €20

Finally, the only additional cost considered is an estimated monthly internet cost of €30/month.

The equipment costs are represented in Table 6-2.

Table 6-2: Cost associated with equipment.

	Total time (months)	Monthly cost (€/month)	Subtotal (€)
Lenovo Legion 15"	4	27,48	109,93
Cell	-	-	20,00
3 thermocouples	-	-	60,00
Climatic chamber	500 hours	1,11/hour	555,00
Battery tester	500 hours	0,56/hour	280,00
DAQ	500 hours	0,64/hour	320,00
Holder	500 hours	-	20,00
Monitor	-	-	10,00
Internet access	4	30	120,00
		Total	**1.494,93**
		Total (VAT incl.)	**2.337,09**

6.3 Software costs

Table 6-3 represents the costs associated with the software packages used for this TFM. For these packages, professional versions are considered.

Microsoft Word, PowerPoint, Teams, and Excel are all part of the 'Microsoft Office 365 Business Standard'-package. This package monthly costs the university €11,70 [85].

Generating figures and calculating are done in MATLAB software. For organizations, the standard license price is €860 each year [86].

In the case of the CFD software ANSYS in which the simulations themselves have been performed, the industrial license cost is €70.000/year, which comes down to an hourly cost of €7,99.

Table 6-3: Cost associated with software packages.

	Total time	**Cost**	**Subtotal (€)**
Microsoft Office 365	4 months	€11,70/month	46,80
MATLAB	4 months	€26,42/month	286,86
ANSYS	200 hours	€7,99/hour	1.598
		Total	**1.931,48**
		Total (VAT incl.)	**2.337,09**

6.4 Budget for material execution

The material execution budget is obtained as the sum of the partial budgets and the indirect costs. An overview is given in Table 6-4.

Table 6-4: Calculation of the budget for material execution.

Human resources	€ 28.190
Equipment	€ 1.494,93
Software	€ 2.337,09
Indirect costs (15%)	€ 4.803,30
Total physical execution	**€ 36.825,33**

6.5 Contract execution budget

The contract execution budget is the sum of the material execution budget and the overhead costs of 13% of this budget. On top of that, a profit of 10% is considered. According to Table 6-5, the total price of this research is € 36.161,37 or € 45.773,88 VAT included.

Table 6-5: Calculation of the contract budget.

Material execution budget	€ 36.825,33
Overhead costs (13%)	€ 4.787,29
Profit (10%)	€ 4.161,26
Contractual implementation (VAT incl.)	**€ 45.773,88**
Contractual implementation	**€ 36.161,37**

References

[1] S. Sepasi, “Adaptive state of charge estimation for battery packs,” 2015.

[2] S. Mathewson, “Experimental Measurements of LiFePO 4 Battery Thermal Characteristics,” 2014.

[3] DNV, “Energy Transition Outlook 2022,” 2022.

[4] McNeil, *An Encyclopedia of the History of Technology*. London: New York Routledge, 2002.

[5] D. Linden and T. B. Reddy, *Handbook of Batteries*. .

[6] H. Abdul-Zehra, “Reserve Batteries.” doi: 10.1007/978-1-349-06319-2_11.

[7] J. Warner, *Lithium-Ion Battery Chemistries*. 2019.

[8] H. Gao, X. Li, and J. Wang, “Lithium Iron Phosphate Battery,” *Encycl. Appl. Electrochem.*, 2014.

[9] C. C. Chan and K. W. E. Cheng, “Lithium Iron Phosphate Batteries,” *Encycl. Sustain. Technol.*, 2017.

[10] J. M. Tarascon and M. Armand, “Lithium Iron Phosphate (LFP) Battery,” *Mater. Sustain. Energy*, 2012.

[11] L. H. Saw, Y. Ye, and A. A. O. Tay, “Electrochemical-thermal analysis of 18650 Lithium Iron Phosphate cell,” *Energy Convers. Manag.*, vol. 75, pp. 162–174, 2013, doi: 10.1016/j.enconman.2013.05.040.

[12] “Understanding Solid Electrolyte Interface (SEI) to Improve Lithium Ion Battery Performance.” https://circuitdigest.com/article/what-is-solid-electrolyte-interface-sei-to-improve-lithium-ion-battery-performance (accessed May 09, 2023).

[13] S. K. Heiskanen, J. Kim, and B. L. Lucht, “Generation and Evolution of the Solid Electrolyte Interphase of Lithium-Ion Batteries,” *Joule*, vol. 3, no. 10, pp. 2322–2333, 2019, doi: 10.1016/j.joule.2019.08.018.

[14] Y. Zhao *et al.*, “A Review on Battery Market Trends, Second-Life Reuse, and Recycling,” *Sustain. Chem.*, vol. 2, no. 1, pp. 167–205, 2021, doi: 10.3390/suschem2010011.

[15] “Battery Anode Market.” https://www.syrahresources.com.au/about/battery-anode-market (accessed May 02, 2023).

[16] “China EV, battery makers grapple with graphite squeeze | Reuters.” https://www.reuters.com/business/autos-transportation/china-ev-battery-makers-grapple-with-graphite-squeeze-2021-12-15/ (accessed Jun. 26, 2023).

[17] S. M. Abu *et al.*, “State of the art of lithium-ion battery material potentials: An analytical evaluations, issues and future research directions,” *J. Clean. Prod.*, vol. 394, Mar. 2023, doi: 10.1016/J.JCLEPRO.2023.136246.

[18] D. Aurbach *et al.*, “Design of electrolyte solutions for Li and Li-ion batteries: a review,” *Electrochim. Acta*, vol. 50, no. 2–3, pp. 247–254, 2004.

[19] N. Anantharamulu, K. Koteswara Rao, G. Rambabu, B. Vijaya Kumar, V. Radha, and M. Vithal, “A wide-ranging review on Nasicon type materials,” *J. Mater. Sci.*, vol. 46, no. 9, p. 2821, May 2011, doi: 10.1007/s10853-011-5302-5.

[20] K. Subramanian *et al.*, “A brief review of recent advances in garnet structured solid electrolyte based lithium metal batteries,” *J. Energy Storage*, vol. 33, Jan. 2021, doi: 10.1016/J.EST.2020.102157.

[21] D. T. Hallinan and N. P. Balsara, “Polymer Electrolytes,” *https://doi.org/10.1146/annurev-*

matsci-071312-121705, vol. 43, pp. 503–525, Jul. 2013, doi: 10.1146/ANNUREV-MATSCI-071312-121705.

[22] S. Chen *et al.*, "Sulfide solid electrolytes for all-solid-state lithium batteries: Structure, conductivity, stability and application," *Energy Storage Mater.*, vol. 14, pp. 58–74, Sep. 2018, doi: 10.1016/J.ENSM.2018.02.020.

[23] "Li-ion batteries, Part 4: Separators - Battery Power Tips." https://www.batterypowertips.com/li-ion-batteries-part-4-separators-faq/ (accessed Jun. 28, 2023).

[24] J. Jang, J. Oh, H. Jeong, W. Kang, and C. Jo, "A review of functional separators for lithium metal battery applications," *Materials (Basel).*, vol. 13, no. 20, pp. 1–37, 2020, doi: 10.3390/ma13204625.

[25] A. Li *et al.*, "A Review on Lithium-Ion Battery Separators towards Enhanced Safety Performances and Modelling Approaches," *Molecules*, vol. 26, no. 478, p. 26020478, 2021.

[26] D. Parikh, T. Christensen, C.-T. Hsieh, and J. Li, "Elucidation of Separator Effect on Energy Density of Li-Ion Batteries," *J. Electrochem. Soc.*, vol. 166, no. 14, pp. A3377–A3383, 2019, doi: 10.1149/2.0571914jes.

[27] J. Warner, *Lithium-ion Battery pack design*. 2015.

[28] P. Zhu, D. Gastol, J. Marshall, R. Sommerville, V. Goodship, and E. Kendrick, "A review of current collectors for lithium-ion batteries," *J. Power Sources*, vol. 485, p. 229321, Feb. 2021, doi: 10.1016/J.JPOWSOUR.2020.229321.

[29] "Current Collectors for Lithium-ion Batteries– MSE Supplies LLC." https://www.msesupplies.com/blogs/news/current-collectors-for-lithium-ion-batteries (accessed May 08, 2023).

[30] Y. Liang *et al.*, "A review of rechargeable batteries for portable electronic devices," *InfoMat*, vol. 1, no. 1, pp. 6–32, Mar. 2019, doi: 10.1002/INF2.12000.

[31] J. W. Choi and D. Aurbach, "Promise and reality of post-lithium-ion batteries with high energy densities," *Nat. Rev. Mater. 2016 14*, vol. 1, no. 4, pp. 1–16, Mar. 2016, doi: 10.1038/natrevmats.2016.13.

[32] W. F. Howard and R. M. Spotnitz, "Theoretical evaluation of high-energy lithium metal phosphate cathode materials in Li-ion batteries," *JPS*, vol. 165, no. 2, pp. 887–891, Mar. 2007, doi: 10.1016/J.JPOWSOUR.2006.12.046.

[33] "Prismatic Cells vs. Cylindrical Cells: What is the Difference? | Laserax." https://www.laserax.com/blog/prismatic-vs-cylindrical-cells (accessed Jun. 28, 2023).

[34] T. Chen *et al.*, "Applications of Lithium-Ion Batteries in Grid-Scale Energy Storage Systems," *Trans. Tianjin Univ.*, vol. 26, pp. 208–217, 1234, doi: 10.1007/s12209-020-00236-w.

[35] C. Vanaclocha Hervas, "Comparative study of three electrochemical cell models for the CFD simulation of a battery module," 2021.

[36] Y. Ji, Y. Zhang, and C. Y. Wang, "Li-ion cell operation at low temperatures," *J. Electrochem. Soc.*, vol. 160, no. 4, pp. A636–A649, 2013, doi: 10.1149/2.047304JES.

[37] A. Pesaran, S. Santhanagopalan, and G.-H. Kim, "Addressing the Impact of Temperature Extremes on Large Format Li-Ion Batteries for Vehicle Applications (Presentation), NREL (National Renewable Energy Laboratory)," 2013.

[38] "How Does Temperature Affect Battery Performance? | Greentech Renewables." https://www.greentechrenewables.com/article/how-does-temperature-affect-battery-

performance (accessed May 11, 2023).

[39] S. Ma *et al.*, “Temperature effect and thermal impact in lithium-ion batteries: A review,” *Prog. Nat. Sci. Mater. Int.*, vol. 28, no. 6, pp. 653–666, Dec. 2018, doi: 10.1016/J.PNSC.2018.11.002.

[40] S. S. Zhang, K. Xu, and T. R. Jow, “The low temperature performance of Li-ion batteries,” *J. Power Sources*, vol. 115, no. 1, pp. 137–140, Mar. 2003, doi: 10.1016/S0378-7753(02)00618-3.

[41] F. Gao and Z. Tang, “Kinetic behavior of LiFePO4/C cathode material for lithium-ion batteries,” *Electrochim. Acta*, vol. 53, no. 15, pp. 5071–5075, Jun. 2008, doi: 10.1016/J.ELECTACTA.2007.10.069.

[42] M. Petzl, M. Kasper, and M. A. Danzer, “Lithium plating in a commercial lithium-ion battery – A low-temperature aging study,” *J. Power Sources*, vol. 275, pp. 799–807, Feb. 2015, doi: 10.1016/J.JPOWSOUR.2014.11.065.

[43] M. Petzl and M. A. Danzer, “Nondestructive detection, characterization, and quantification of lithium plating in commercial lithium-ion batteries,” *J. Power Sources*, vol. 254, pp. 80–87, May 2014, doi: 10.1016/J.JPOWSOUR.2013.12.060.

[44] V. Zinth *et al.*, “Lithium plating in lithium-ion batteries at sub-ambient temperatures investigated by in situ neutron diffraction,” *J. Power Sources*, vol. 271, pp. 152–159, Dec. 2014, doi: 10.1016/J.JPOWSOUR.2014.07.168.

[45] N. Gunawardhana, N. Dimov, M. Sasidharan, G. J. Park, H. Nakamura, and M. Yoshio, “Suppression of lithium deposition at sub-zero temperatures on graphite by surface modification,” *Electrochem. commun.*, vol. 13, no. 10, pp. 1116–1118, Oct. 2011, doi: 10.1016/J.ELECOM.2011.07.014.

[46] M. Xiao and S. Y. Choe, “Theoretical and experimental analysis of heat generations of a pouch type LiMn2O4/carbon high power Li-polymer battery,” *J. Power Sources*, vol. 241, pp. 46–55, Nov. 2013, doi: 10.1016/J.JPOWSOUR.2013.04.062.

[47] D. Bernardi, E. Pawlikowski, and J. Newman, “GENERAL ENERGY BALANCE FOR BATTERY SYSTEMS.,” *Electrochem. Soc. Ext. Abstr.*, vol. 84–2, no. 1, pp. 164–165, Jan. 1984, doi: 10.1149/1.2113792/XML.

[48] W. Lu and J. Prakash, “In Situ Measurements of Heat Generation in a Li/Mesocarbon Microbead Half-Cell,” *J. Electrochem. Soc.*, vol. 150, no. 3, pp. A262–A266, Mar. 2003, doi: 10.1149/1.1541672.

[49] M. Balasundaram, V. Ramar, C. Yap, L. Lu, A. A. O. Tay, and B. Palani, “Heat loss distribution: Impedance and thermal loss analyses in LiFePO4/graphite 18650 electrochemical cell,” *J. Power Sources*, vol. 328, pp. 413–421, Oct. 2016, doi: 10.1016/J.JPOWSOUR.2016.08.045.

[50] A. Nyman, T. G. Zavalis, R. Elger, M. Behm, and G. Lindbergh, “Analysis of the Polarization in a Li-Ion Battery Cell by Numerical Simulations,” *J. Electrochem. Soc.*, vol. 157, no. 11, p. A1236, 2010, doi: 10.1149/1.3486161.

[51] X. Zhang, “Thermal analysis of a cylindrical lithium-ion battery,” *Electrochim. Acta*, vol. 56, no. 3, pp. 1246–1255, Jan. 2011, doi: 10.1016/J.ELECTACTA.2010.10.054.

[52] X. G. Yang, G. Zhang, and C. Y. Wang, “Computational design and refinement of self-heating lithium ion batteries,” *J. Power Sources*, vol. 328, pp. 203–211, Oct. 2016, doi: 10.1016/J.JPOWSOUR.2016.08.028.

[53] B. Yan, C. Lim, L. Yin, and L. Zhu, “Simulation of heat generation in a reconstructed LiCoO2 cathode during galvanostatic discharge,” *Electrochim. Acta*, vol. 100, pp. 171–179, Jun. 2013, doi: 10.1016/J.ELECTACTA.2013.03.132.

[54] J. Esmaeili and H. Jannesari, “Developing heat source term including heat generation at rest condition for Lithium-ion battery pack by up scaling information from cell scale,” *Energy Convers. Manag.*, vol. 139, pp. 194–205, May 2017, doi: 10.1016/J.ENCONMAN.2017.02.052.

[55] T. Ohsaki *et al.*, “Overcharge reaction of lithium-ion batteries,” *J. Power Sources*, vol. 146, no. 1–2, pp. 97–100, Aug. 2005, doi: 10.1016/J.JPOWSOUR.2005.03.105.

[56] Q. Wang, P. Ping, X. Zhao, G. Chu, J. Sun, and C. Chen, “Thermal runaway caused fire and explosion of lithium ion battery,” *J. Power Sources*, vol. 208, pp. 210–224, Jun. 2012, doi: 10.1016/J.JPOWSOUR.2012.02.038.

[57] M. Xu, B. Reichman, and X. Wang, “Modeling the effect of electrode thickness on the performance of lithium-ion batteries with experimental validation,” *Energy*, vol. 186, p. 115864, Nov. 2019, doi: 10.1016/J.ENERGY.2019.115864.

[58] D. Li *et al.*, “The Effect of Electrode Thickness on the High-Current Discharge and Long-Term Cycle Performance of a Lithium-Ion Battery,” *Batter. 2022, Vol. 8, Page 101*, vol. 8, no. 8, p. 101, Aug. 2022, doi: 10.3390/BATTERIES8080101.

[59] D. Y. W. Yu, K. Donoue, T. Inoue, M. Fujimoto, and S. Fujitani, “Effect of Electrode Parameters on LiFePO[sub 4] Cathodes,” *J. Electrochem. Soc.*, vol. 153, no. 5, p. A835, Mar. 2006, doi: 10.1149/1.2179199/XML.

[60] H. Zheng, J. Li, X. Song, G. Liu, and V. S. Battaglia, “A comprehensive understanding of electrode thickness effects on the electrochemical performances of Li-ion battery cathodes,” *Electrochim. Acta*, vol. 71, pp. 258–265, Jun. 2012, doi: 10.1016/J.ELECTACTA.2012.03.161.

[61] C. X. Ding, Q. S. Meng, L. Wang, and C. H. Chen, “Synthesis, structure, and electrochemical characteristics of LiNi1/3Co1/3Mn1/3O2 prepared by thermal polymerization,” *Mater. Res. Bull.*, vol. 44, no. 3, pp. 492–498, Mar. 2009, doi: 10.1016/J.MATERRESBULL.2008.08.012.

[62] J. W. Lee, J. H. Lee, T. T. Viet, J. Y. Lee, J. S. Kim, and C. H. Lee, “Synthesis of LiNi1/3Co1/3Mn1/3O2 cathode materials by using a supercritical water method in a batch reactor,” *Electrochim. Acta*, vol. 55, no. 8, pp. 3015–3021, Mar. 2010, doi: 10.1016/J.ELECTACTA.2009.12.080.

[63] M. F. Lagadec, R. Zahn, and V. Wood, “Characterization and performance evaluation of lithium-ion battery separators,” *Nat. Energy 2018 41*, vol. 4, no. 1, pp. 16–25, Dec. 2018, doi: 10.1038/s41560-018-0295-9.

[64] E. Lizundia, C. M. Costa, R. Alves, and S. Lanceros-Méndez, “Cellulose and its derivatives for lithium ion battery separators: A review on the processing methods and properties,” *Carbohydr. Polym. Technol. Appl.*, vol. 1, p. 100001, Dec. 2020, doi: 10.1016/J.CARPTA.2020.100001.

[65] D. V. Horváth, R. Tian, C. Gabbett, V. Nicolosi, and J. N. Coleman, “Quantifying the Effect of Separator Thickness on Rate Performance in Lithium-Ion Batteries,” *J. Electrochem. Soc.*, vol. 169, no. 3, p. 030503, Mar. 2022, doi: 10.1149/1945-7111/AC5654.

[66] A. Bhargav, J. He, A. Gupta, and A. Manthiram, “Lithium-Sulfur Batteries: Attaining the Critical Metrics,” *Joule*, vol. 4, no. 2, pp. 285–291, Feb. 2020, doi: 10.1016/j.joule.2020.01.001.

[67] J. Liu *et al.*, “Pathways for practical high-energy long-cycling lithium metal batteries,” *Nat. Energy*, vol. 4, no. 3, pp. 180–186, Mar. 2019, doi: 10.1038/S41560-019-0338-X.

[68] S. Dörfler, H. Althues, P. Härtel, T. Abendroth, B. Schumm, and S. Kaskel, “Challenges and Key Parameters of Lithium-Sulfur Batteries on Pouch Cell Level,” *Joule*, vol. 4, no. 3, pp. 539–554, Mar. 2020, doi: 10.1016/j.joule.2020.02.006.

[69] S. H. Chung and A. Manthiram, “Designing Lithium-Sulfur Cells with Practically Necessary Parameters,” *Joule*, vol. 2, no. 4, pp. 710–724, Apr. 2018, doi: 10.1016/j.joule.2018.01.002.

[70] R. Choudhury, J. Wild, and Y. Yang, “Engineering current collectors for batteries with high specific energy,” *Joule*, vol. 5, no. 6, pp. 1301–1305, Jun. 2021, doi: 10.1016/J.JOULE.2021.03.027.

[71] S. Jin *et al.*, “Advanced 3D Current Collectors for Lithium-Based Batteries,” *Adv. Mater.*, vol. 30, no. 48, p. 1802014, Nov. 2018, doi: 10.1002/ADMA.201802014.

[72] “Specification for Lithium-ion Rechargeable Cell.” OPTIMUMNANO ENERGY CO., LTD, p. 10, 2020.

[73] “cross-section-spirally-wound-jelly-roll.png (1670×686).” https://cdn.comsol.com/wordpress/sites/1/2022/03/cross-section-spirally-wound-jelly-roll.png (accessed Jun. 12, 2023).

[74] T. Bergmann, A. Lavine, F. Incropera, and D. Dewitt, *HEAT and MASS TRANSFER*. John Wiley & Sons, Ltd, 2011.

[75] G.-H. Kim, K. Smith, K.-J. Lee, S. Santhanagopalan, and A. Pesaran, “Multi-Domain Modeling of Lithium-Ion Batteries Encompassing Multi-Physics in Varied Length Scales,” *J. Electrochem. Soc.*, vol. 158, no. 8, p. A955, 2011, doi: 10.1149/1.3597614.

[76] ANSYS, *Ansys Fluent Theory Guide*. 2021.

[77] A. Melcher, C. Ziebert, M. Rohde, B. Lei, and H. Ju, “ECM Models for Li-Ion Batteries – A Short Mathematical Survey and Simulations Equivalent Circuit Models for Li-ion Batteries,” pp. 53–58.

[78] B. Yann Liaw, R. G. Jungst, A. Urbina, and T. L. Paez, “Modeling of Battery Life I. The Equivalent Circuit Model (ECM) Approach,” *Sandia Natl. Lab.*, p. 6, 2003, [Online]. Available: http://www.sandia.gov/ess/EESAT/2003_papers/Liaw.pdf.

[79] A. Broatch, P. Olmeda, X. Margot, and L. Agizza, “A generalized methodology for lithium-ion cells characterization and lumped electro-thermal modelling,” *Appl. Therm. Eng.*, vol. 217, no. April, p. 119174, 2022, doi: 10.1016/j.applthermaleng.2022.119174.

[80] L. Wang *et al.*, “Unlocking the significant role of shell material for lithium-ion battery safety,” *Mater. Des.*, vol. 160, pp. 601–610, Dec. 2018, doi: 10.1016/J.MATDES.2018.10.002.

[81] J. Kang, Y. Jia, G. Zhu, J. V. Wang, B. Huang, and Y. Fan, “How electrode thicknesses influence performance of cylindrical lithium-ion batteries,” *J. Energy Storage*, vol. 46, p. 103827, Feb. 2022, doi: 10.1016/J.EST.2021.103827.

[82] E. Gümüşsu, Ö. Ekici, and M. Köksal, “3-D CFD modeling and experimental testing of thermal behavior of a Li-Ion battery,” *Appl. Therm. Eng.*, vol. 120, pp. 484–495, Jun. 2017, doi: 10.1016/J.APPLTHERMALENG.2017.04.017.

[83] “Tax Agency:VAT tax rates.” https://sede.agenciatributaria.gob.es/Sede/en_gb/iva/calculo-iva-repercutido-clientes/tipos-impositivos-iva.html (accessed Jun. 29, 2023).

[84] “Credit - Educational glossary.” https://www.kuleuven.be/english/education/educational-glossary/educational-glossary-c/credit (accessed Jun. 28, 2023).

[85] “Comparar todos los planes de Microsoft 365 | Microsoft.” https://www.microsoft.com/es-es/microsoft-365/business/compare-all-microsoft-365-business-products?&activetab=tab:primaryr2 (accessed Jul. 01, 2023).

[86] “Pricing and Licensing - MATLAB & Simulink.” https://es.mathworks.com/pricing-licensing.html?prodcode=ML&intendeduse=edu (accessed May 31, 2023).

List of tables

List of figures

ESCOLA TECNICA SUPERIOR ENGINYERIA INDUSTRIAL VALENCIA
UNIVERSITAT POLITECNICA DE VALENCIA
Camí de Vera s/n – Edificio 5F
46022 VALÈNCIA, España
tel. + 34 963 87 71 70
informatica@etsii.upv.es
https://www.etsii.upv.es/